235 (2024) 212634

Contents lists available at ScienceDirect

Geoenergy Science and Engineering

journal homepage: www.sciencedirect.com/journal/geoenergy-science-and-engineering

Acoustical-electrical models of tight rocks based on digital rock physics and double-porosity theory

Mengqiang Pang [a,b], Martin Balcewicz [b], Jing Ba [a,*], José M. Carcione [a,c], Mirko Siegert [b], Erik H. Saenger [b,d,e]

[a] School of Earth Sciences and Engineering, Hohai University, Nanjing, 211100, China
[b] Hochschule Bochum, Am Hochschulcampus 1, 44801, Bochum, Germany
[c] National Institute of Oceanography and Applied Geophysics – OGS, Trieste, 34010, Italy
[d] Fraunhofer IEG - Institution for Energy Infrastructures and Geothermal Energy, Am Hochschulcampus 1, 44801, Bochum, Germany
[e] Institute of Geology, Mineralogy, and Geophysics, Ruhr-University Bochum, Universitätsstrasse 150, 44801, Bochum, Germany

ARTICLE INFO

Keywords:
Digital rock physics
Equivalent petrophysical model
Tight-oil rock
Pore structure
Acoustic and electrical properties
Permeability

ABSTRACT

The acoustical-electrical (AE) properties of reservoir rocks are affected by their microstructure (pores, micro-fractures, cracks and their geometry) and saturating fluids. To aid the interpretation, digital rock physics (DRP) is a useful technique to characterize this microstructure, as well as equivalent petrophysical models (EPM) to obtain joint AE properties. We perform thin-section analysis on rocks from tight-oil reservoirs, along with X-ray diffraction (XRD) and computed tomography (CT) to study rock lithology and minerals. We also perform porosity, permeability, ultrasound, and electrical conductivity experiments as a function of confining pressure to analyze pore structure. First, the 3D digital multicomponent cores are created based on a geology-driven multiphase segmentation workflow and images of the samples, and verified based on the porosity and minerals. Then, the AE properties and permeability are calculated by using numerical simulations (finite difference and finite volume methods). Next, the rigid and microcracked (soft) porosities are determined by using the Shapiro model to create the rock skeleton. We develop a joint EPM based on the effective medium AE and the Biot-Rayleigh equations with double porosity to describe the rock properties. The ultrasonic, sonic and seismic multiple data are used to compare and analyze the two approaches. The results show that the DRP techniques based on real cores are effective in characterizing the microstructure and the proposed EPM can describe the AE properties of real rocks, indicating a potential for quantitative characterization of reservoirs.

1. Introduction

The pore structure of reservoir rocks involves the geometry, size, distribution, and connectivity of pores and throats, which compose the main space for hydrocarbon storage and transport. Theoretical and experimental studies have shown that pore and throat systems significantly affect the physical properties (Müller et al., 2010; Amalokwu et al., 2014; Chapman et al., 2016; Zhang et al., 2021, 2022; Wang et al., 2021, 2022a; Luo et al., 2023), such as permeability, acoustic velocities and electrical properties and the related wave attenuation (Solazzi et al., 2019; Ba et al., 2017; Sun et al., 2019; Pang et al., 2021a, 2021b; Guo et al., 2022a, 2022b). Thus, an in-depth analysis of how the pore structure affects the AE properties is significant for reservoir characterization.

DRP has become a complementary approach for imaging reservoir rocks. By using X-ray computed tomography (CT), minerals, and geometric and volumetric properties, are imaged on a location-dependent volume (Wildenschild et al., 2002; Andrä et al., 2013a; Blunt et al., 2013; Madonna et al., 2013; Zhou et al., 2016, 2017; Kadyrov et al., 2022). The imaged phase differences, which appear as gray-scale intensities, are processed by considering X-ray artifacts and segmented into binary files (Schlüter et al., 2014; Karimpouli et al., 2020; Alqahtani et al., 2021; Balcewicz et al., 2021). Then, physical properties are computed, such as, effective elastic and hydraulic properties, and thermal conductivity (Saenger et al., 2000, 2005, 2016; Andrä et al., 2013b; Saxena et al., 2019; Siegert et al., 2022; Wang et al., 2022b). This method has found wide application, particularly in the study of porosities and permeabilities associated with multiphase flows (Spurin et al.,

* Corresponding author.
E-mail address: jba@hhu.edu.cn (J. Ba).

https://doi.org/10.1016/j.geoen.2024.212634
Received 3 May 2023; Received in revised form 15 November 2023; Accepted 2 January 2024
Available online 7 January 2024

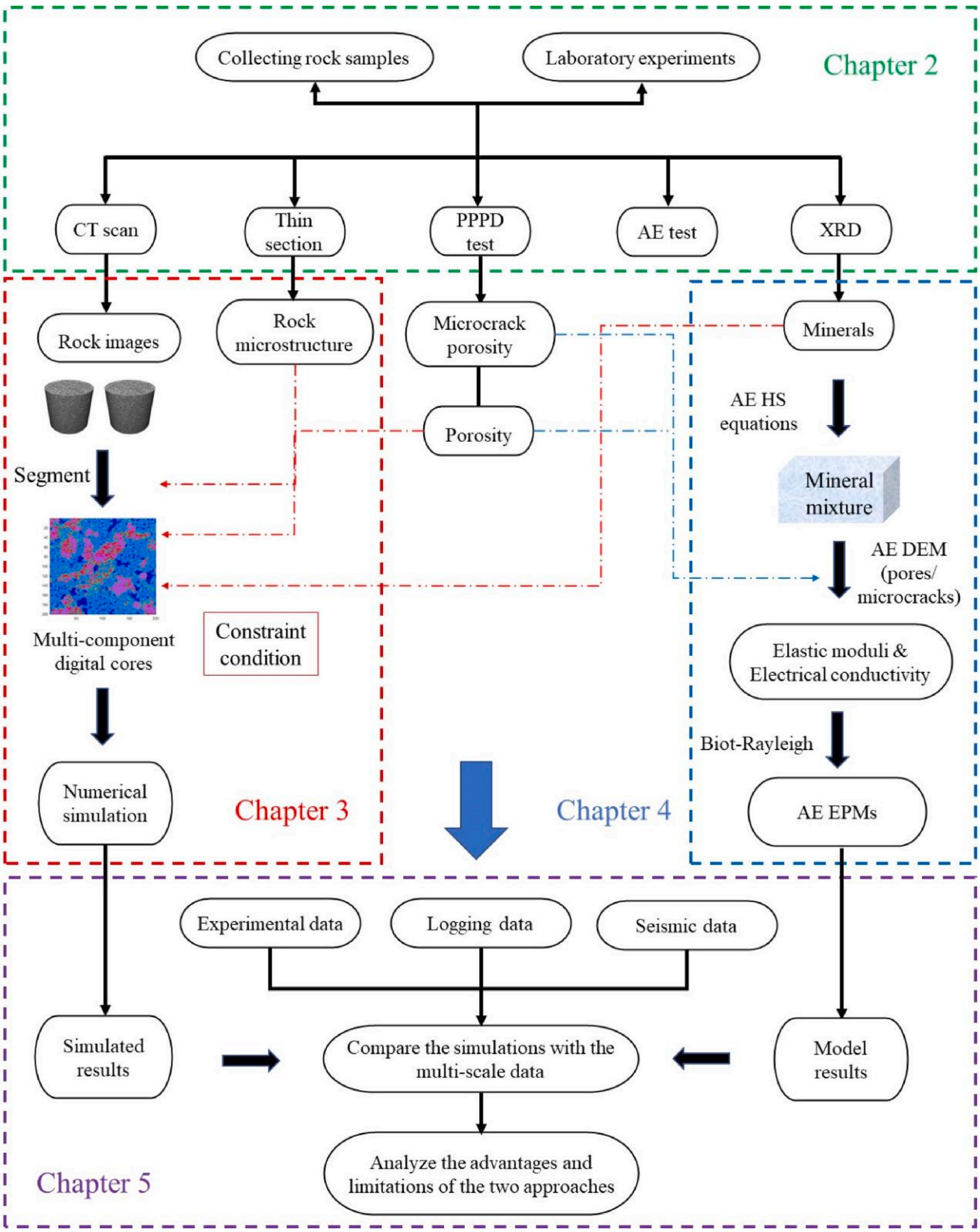

Fig. 1. The flowchart of this work.

Table 1
Properties of the rock samples.

Samples	A	B	C	D
Depth (m)	1949.4	2011.8	1994	2121.26
Porosity (%)	5.787	7.220	9.0002	8.998
Permeability (mD)	0.020	0.020	0.036	0.078
Dry-rock density (g/cm^3)	2.514	2.492	2.417	2.415

2023; Bultreys et al., 2022), capillary pressure (Paustian et al., 2021), and in areas such as hydrogen storage (Jangda et al., 2023) and the general problem of upscaling (Menke et al., 2021). Advances in computational power have also facilitated the use of convolutional neural networks (CNN) in automatic grayscale assignment (SaxenaDay-Stirrat et al., 2021). However, the resolution of the scanned microstructure remains a challenge. For example, CNN can be used to scale low-resolution XRCT volumes to high resolution in DRP (Karimpouli and Kadyrov, 2022). Recent 3D observations demonstrate the impact that advances in general scan time can have on poorly

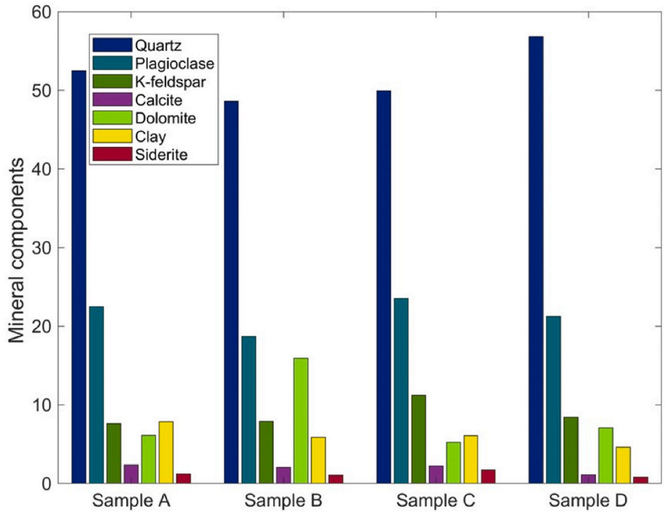

Fig. 2. Mineral components of the samples.

understood processes. Accordingly, contemporaneous in situ X-ray imaging can provide new insights into shear failure of porous rocks (Cartwright-Taylor et al., 2022). Li et al. (2020) analyzed the effect of fluid saturation and pore structure on electrical properties based on 3D digital cores with multiple mineral fractions by using the finite element method (FEM) and laboratory tests. Tan et al. (2021) constructed the digital samples of carbonates to study the effects of openness, lengths, aspect ratios, and densities of microfractures on the elastic attributes by using CT scan and FEM.

Many theories are widely used to evaluate pore structure, mineral components and pore fluids from AE properties (Carcione and Avseth, 2015; Picotti et al., 2018; Pang et al., 2019, 2022), in particular equivalent medium theories, based on the simplified assumptions (Golikov et al., 2012; Ba et al., 2013a, 2013b; Deng et al., 2015). For example, Gupta et al. (2012) obtained an isobath map of sandstone reservoirs in the Cambay Basin by establishing an equivalent petrophysical model (EPM) based on the Kuster-Toksöz theory. Jensen et al. (2013) used the differential equivalent medium (DEM) theory and calibrated the model with core and logging data.

It has become a standard technique to use joint AE properties for evaluating pore structure, fluid saturation, and fracture content (Carcione et al., 2007, 2012; Gabàs et al., 2016; Cilli and Chapman, 2021;

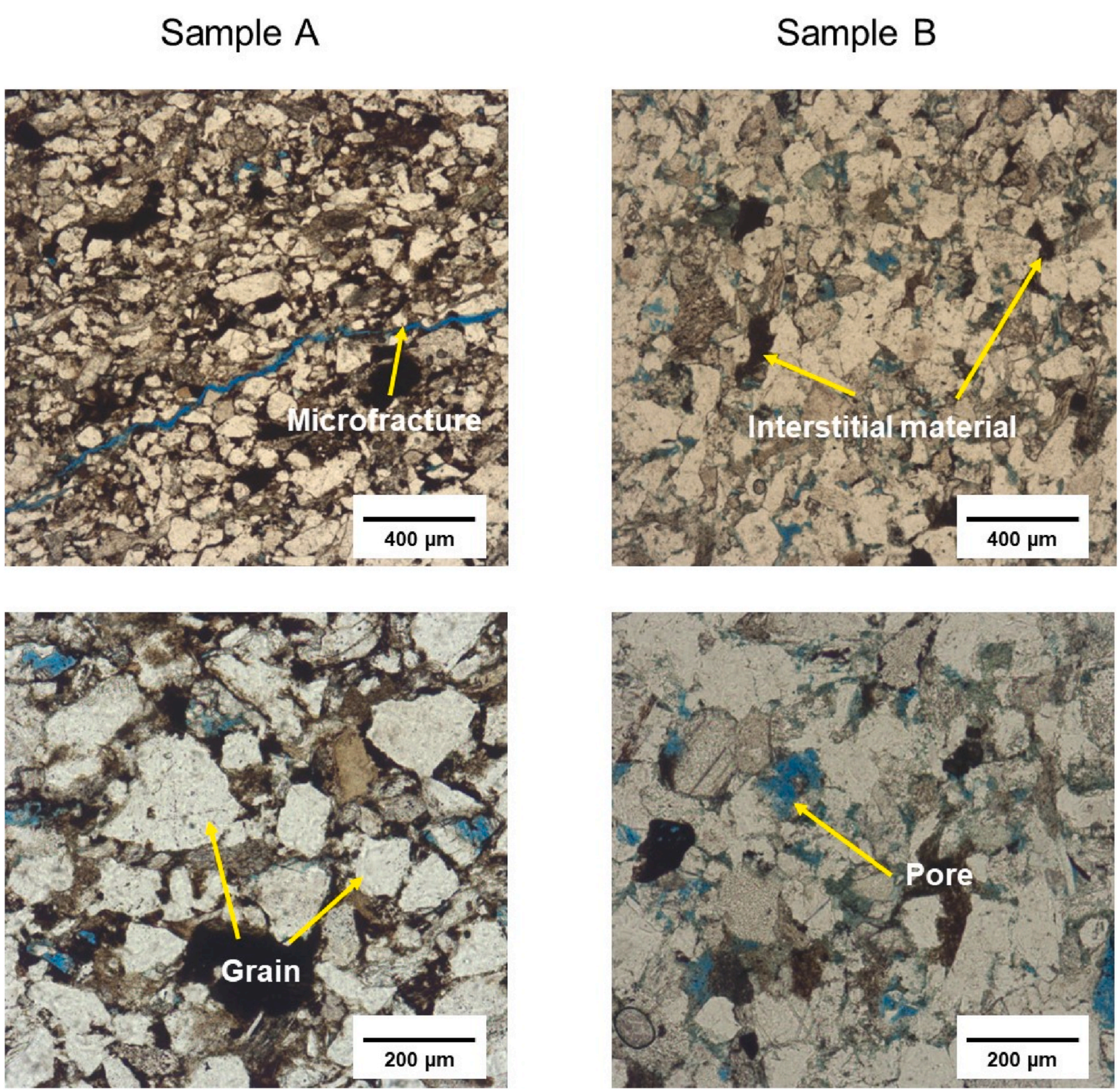

Fig. 3. Stained thin sections with blue epoxy of samples A and B at different scales indicating the mineral grains and small pore voids in blue.

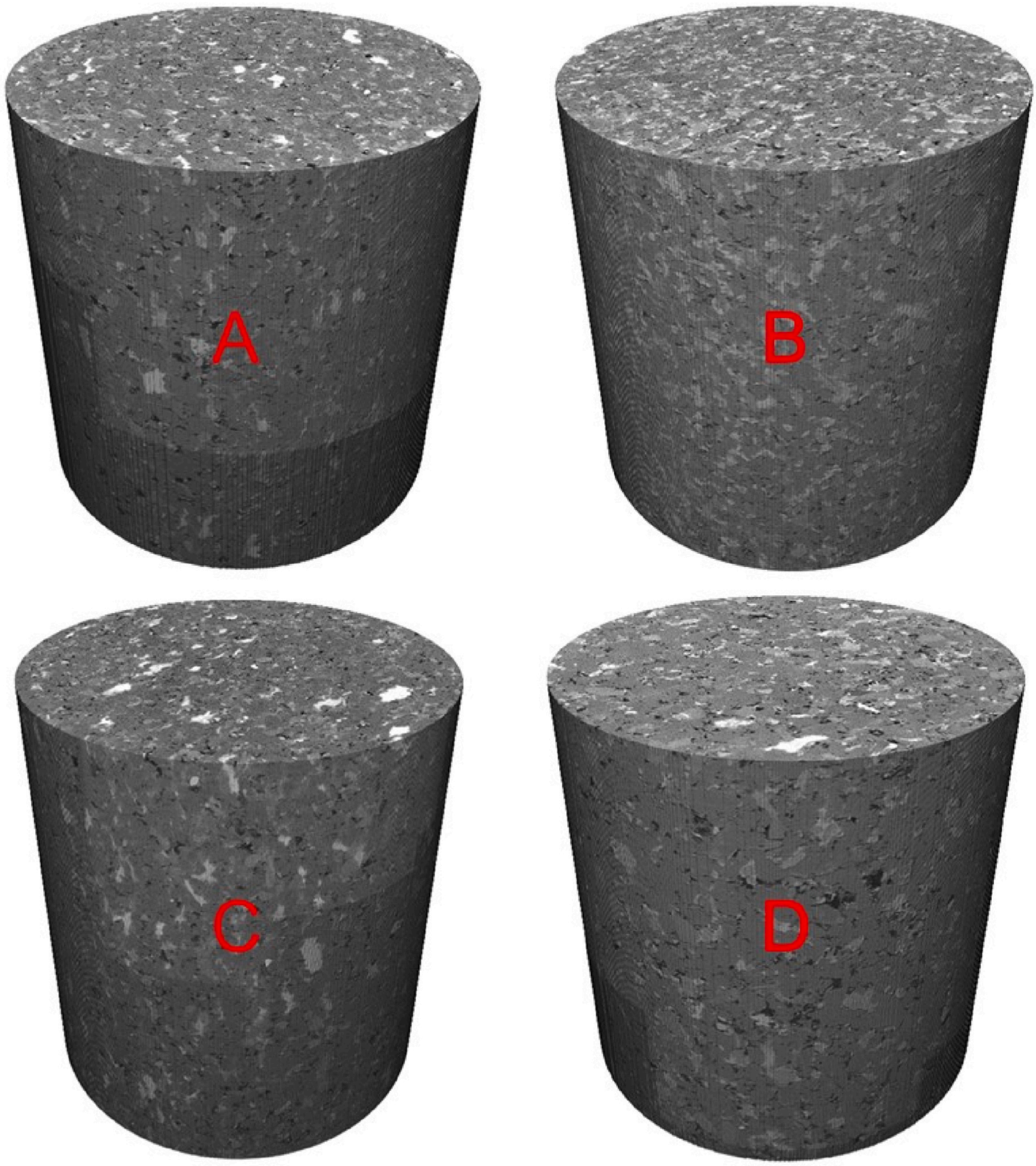

Fig. 4. Computed Tomography (CT) images of samples A-D. The diameter and length are 5 mm.

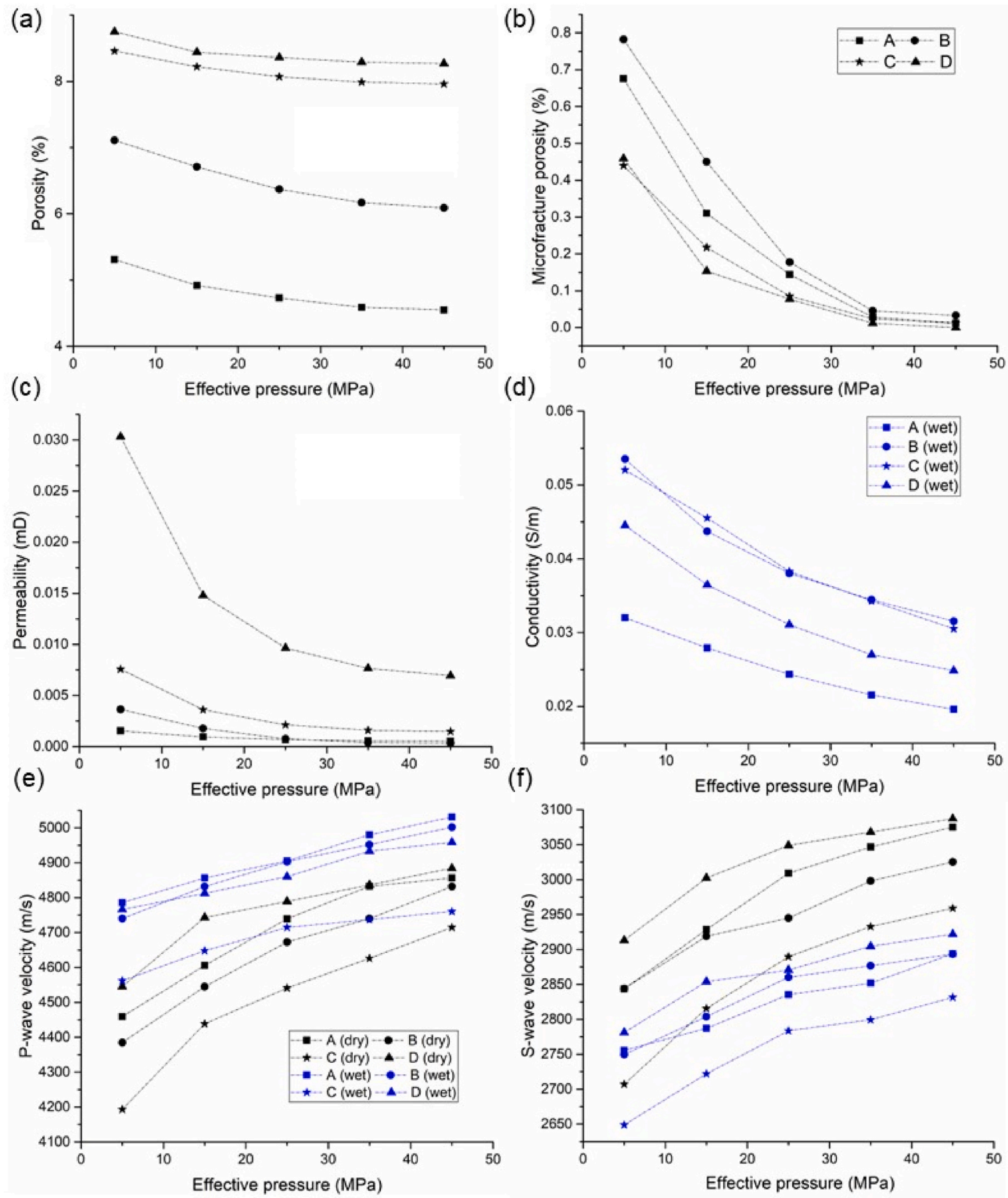

Fig. 5. Porosity (a), microfracture-crack (soft) porosity (b), permeability (c), conductivity (d), P-wave velocity (e), and S-wave (f) velocity as a function of effective pressure for samples A-D.

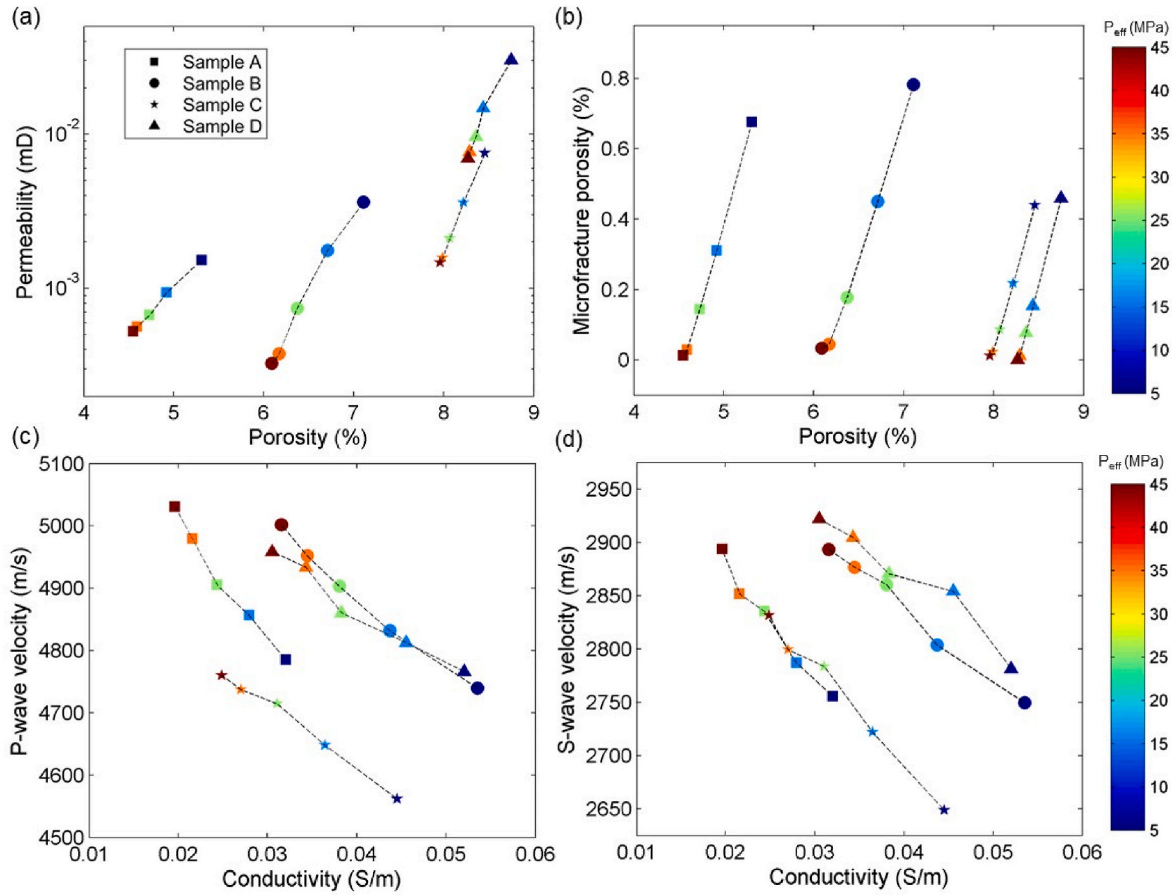

Fig. 6. Cross-property relations. Permeability (a) and soft porosity (b) versus total porosity. P- (c) and S-wave (d) velocities versus conductivity. Color represents effective pressure.

Han et al., 2011, 2018, 2020). Cilli and Chapman (2020) analyzed resistivity and elastic moduli based on a power-law relationship between porosity and grain or pore aspect ratio, which was validated by laboratory measurements on carbonate samples. Pang et al. (2021a, 2022) constructed 3D AE models for tight-oil reservoirs to characterize the microstructure of subsurface formations by using experimental and well-log data.

Tight oil refers to oil that accumulates in source rocks in a free or adsorbed state or in dense sandstones and carbonates interbedded with or adjacent to source rocks (Jia et al., 2012). In general, this oil accumulation has not yet experienced large-scale and long-range migration (Ma et al., 2019). Compared to conventional reservoir rocks, tight-oil rocks have complex characteristics of lithology and structure, with small pore throats and sizes, multiple pore types, and large specific surface area (Wang et al., 2015; Pang et al., 2021b). Given the complex characteristics of lithology and microstructure, we develop DRP and EPM approaches using multiple rock physics experiments based on conventional modeling techniques.

The flow diagram for this work is shown in Fig. 1. In the study, cores are collected from a tight-oil reservoir in the Ordos Basin, western China, and CT scans, XRD, thin sections, porosity, permeability, ultrasonic waveforms, and electrical conductivity of the samples are determined. Based on CT images and thin sections, multi-component 3D digital samples are created, calibrated and constrained by porosity and mineral analysis. Then numerical simulations are performed to compute the effective AE properties and permeability. Stiff and soft pores and mineral compositions are determined by pressure-dependent porosity and XRD experiments, respectively. Then, we develop a joint EPM to obtain the AE properties based on effective medium theory and the Biot-Rayleigh acoustic wave equations with double porosity (Ba et al., 2011). Finally, the simulated results of the two methods are compared with laboratory and field data.

2. Core samples and laboratory experiments

Rich hydrocarbon resources have been developed in the Yanchang Formations of the Q area of Ordos basin, characterized by complex tectonic activities and high-quality source rocks (Liu et al., 2021). The tight-oil reservoir of the 7th member of the Yanchang Formation is mainly deposited in lacustrine facies (Shi et al., 2022; Ji et al., 2022), and the burial depth is between 1200 and 2350 m, which is the layer in this study. We extract four cores (samples A-D) from the layer, at depths between 1950 and 2150 m, where the formation pore and effective pressures are approximately 15 MPa. Subsamples are obtained with diameters ranging from 25.08 to 25.13 mm and lengths ranging from 49.05 to 49.77 mm. The physical properties of the samples are given in Table 1.

2.1. Thin section, XRD and CT tests

We perform XRD measurements to analyze the mineral fractions of the samples (Fig. 2). The sandstone samples are composed mainly of quartz, feldspar, and small amounts of carbonates, clay, and siderite. Plagioclase or potassium feldspars are observed, where the former is a major constituent. The carbonate minerals are mainly calcite and dolomite. Fig. 3 shows thin sections of samples A and B at different

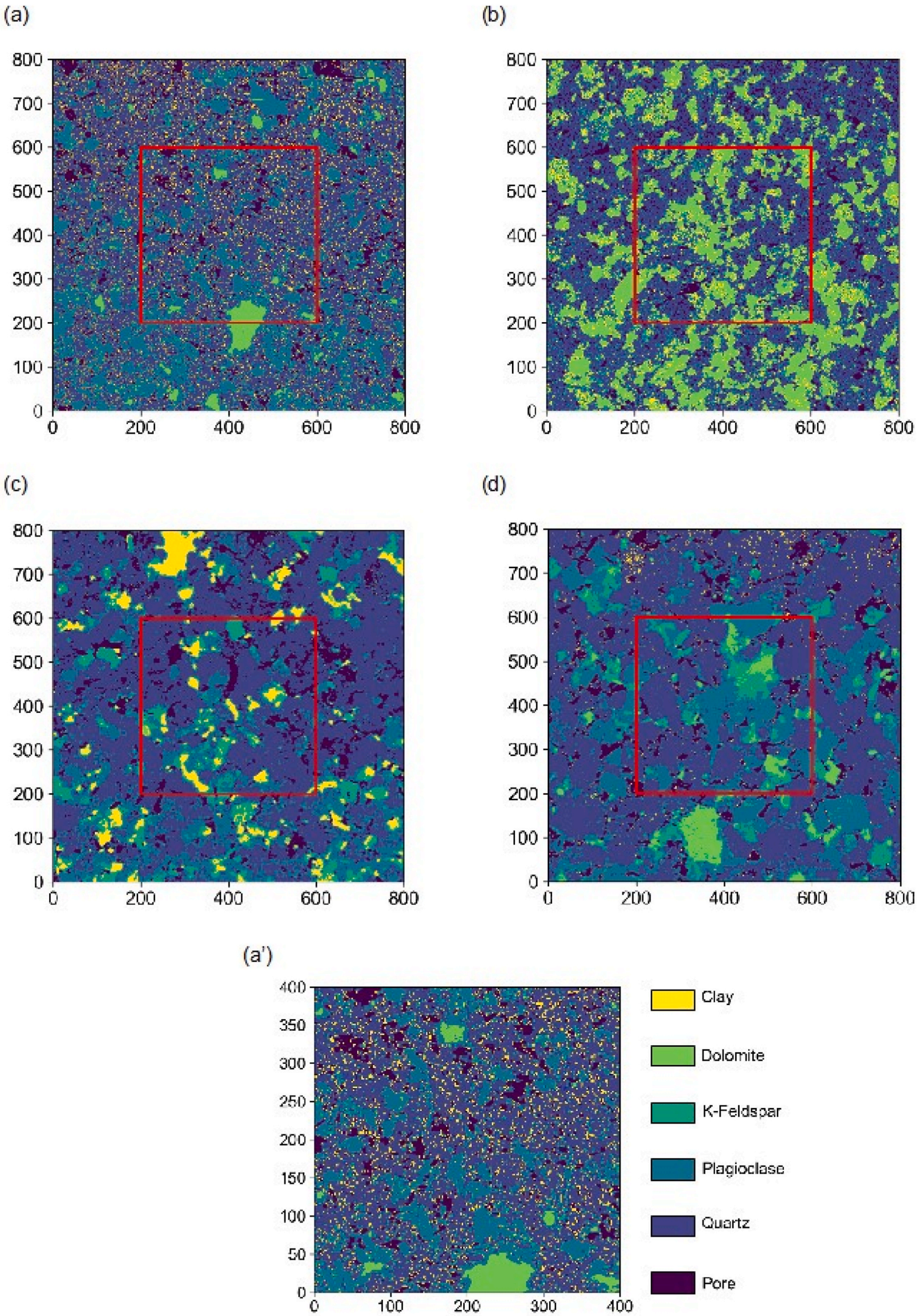

Fig. 7. Image segmentation of samples A-D. Panel (a') corresponds to a blow up of sample A.

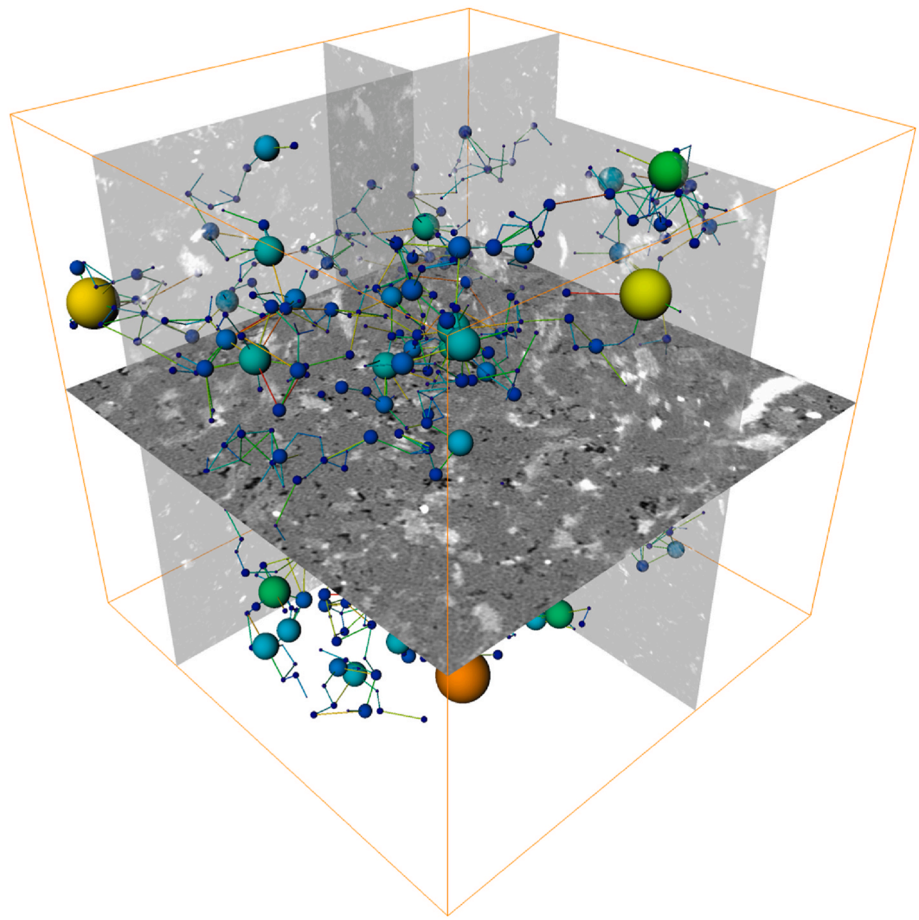

Fig. 8. Connected pore space of sample A represented as a lattice of wide pores (shown as spheres) connected by pore throats (shown as cylinders). The color of the pore or throat indicates the volume and channel length, respectively.

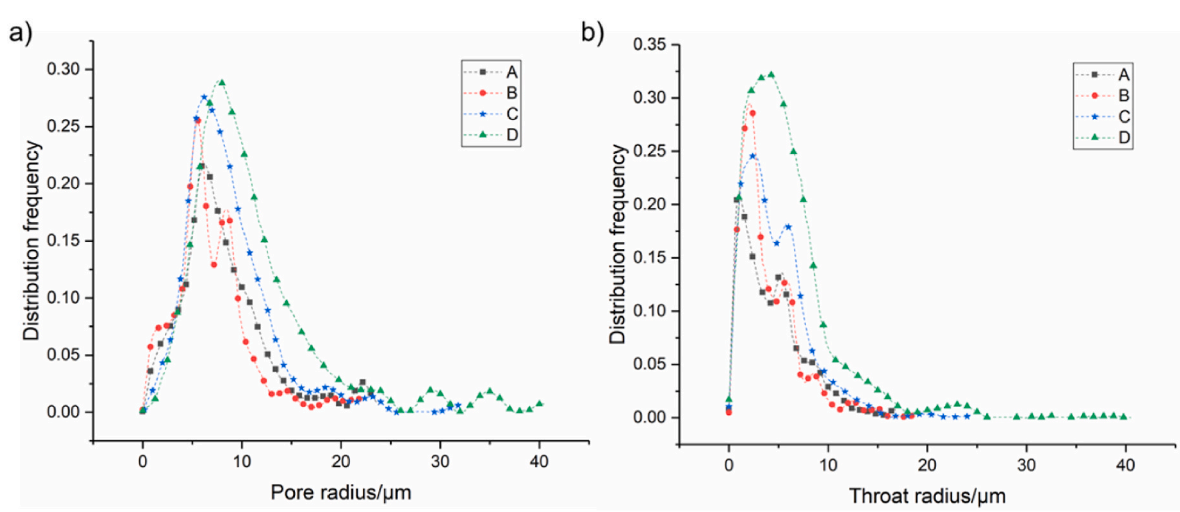

Fig. 9. Distributions of the pore (a) and throat (b) radii of the samples.

Table 2
Simulated permeability and AE properties.

Samples		A		B		C		D	
Simulated results	Direction	κ mD	σ S/m	κ mD	σ S/m	κ mD	σ S/m	κ mD	σ S/m
	X	/	0.001616	0.16	0.000813	1.39	0.00302	2.67	0.00466
	Y	0.06	0.004708	0.48	0.00184	7.90	0.01184	1.46	0.00345
	Z	0.05	0.01375	0.23	0.00093	0.10	0.001	1.47	0.00302
	Z	V_P m/s	V_S m/s	V_P m/s	V_S m/s	V_P m/s	V_S m/s	V_P m/s	V_S m/s
		4728	2844	5071	3014	4809	2948	5008	3089

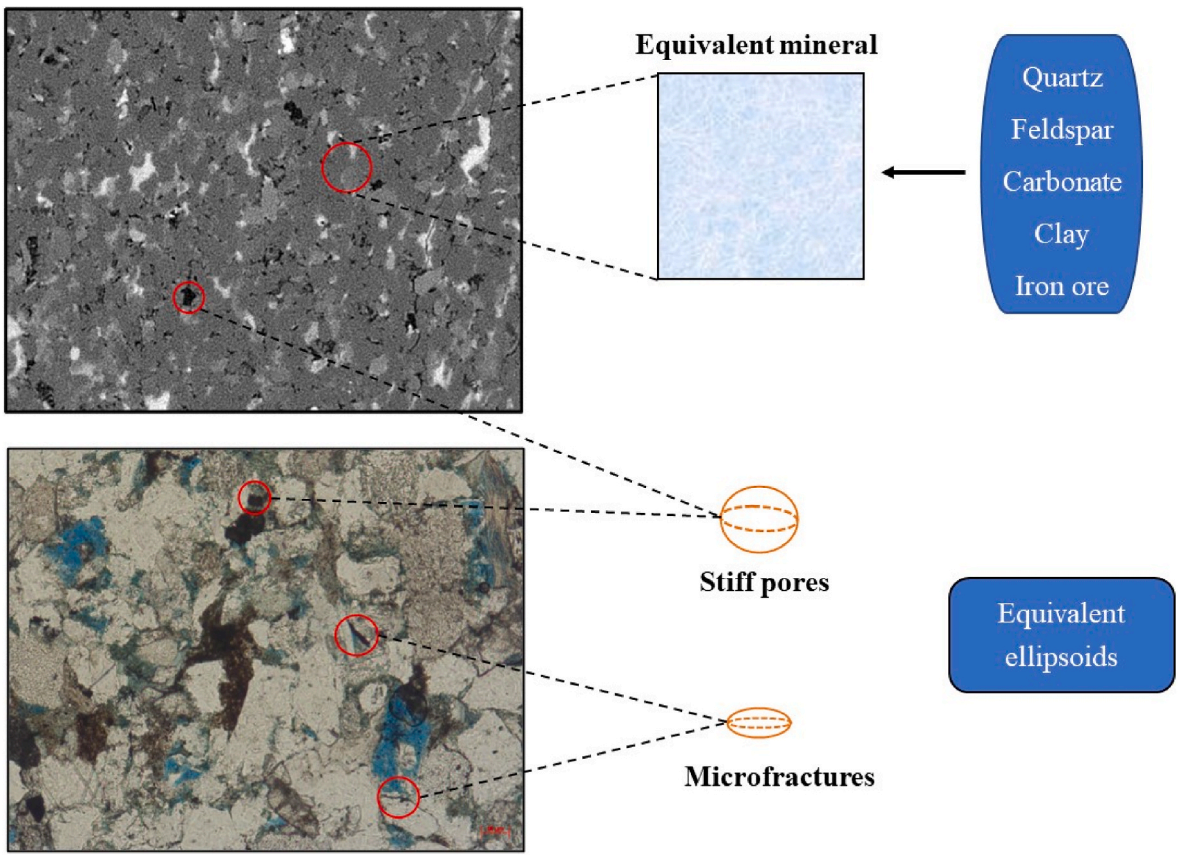

Fig. 10. Diagram of the rock microstructure and equivalent model.

Table 3
Material properties.

Grain bulk modulus (K_S)	37 GPa
Grain shear modulus (G_S)	44 GPa
Grain density (ρ_S)	2.65 g/cm^3
Water bulk modulus (K_W)	2.24 GPa
Water density (ρ_W)	1.002 g/cm^3
Water viscosity (η_W)	0.00098 Pa s
Oil bulk modulus (K_O)	1.27 GPa
Oil density (ρ_O)	0.8 g/cm^3
Oil viscosity (η_O)	0.0021 Pa s
Gas bulk modulus (K_g)	0.018 GPa
Gas density (ρ_g)	0.09 g/cm^3
Gas viscosity (η_g)	0.000016 Pa s
Grain conductivity (σ_S)	0.15 S/m
Water conductivity (σ_W)	8.7 S/m
Lithology coefficient (γ)	1
Saturation exponent (n)	2
Pore aspect ratio (α_0)	0.5
Crack aspect ratio (α_C)	0.001
Inclusion porosity (φ_{20})	0.01
Inclusion radius (R_0)	0.1 mm
Inclusion aspect ratio	1

scales, indicating a tight rock with small pore voids. Here, intergranular and dissolved pores and microfractures are mainly considered. The small-sized samples (diameter and length of 5 mm) are processed for CT scans, and the images are given in Fig. 4, with a voxel resolution of 2.8 × 2.8 × 2.8 μm. The CT datasets provided are in an 8-bit format, resulting in gray-scale intensities from 0 to 255.

2.2. Porosity, permeability and AE tests

Porosity and permeability pressure-dependent (PPPD) tests are performed at confining pressures of 20, 30, 40, 50 and 60 MPa and a pore pressure of 15 MPa. Then, ultrasonic P- and S-wave velocities are determined by the ultrasonic pulse method. The specimens are oven-dried and then saturated with water under pressure. The measurements are performed at the above pressures and at 0.55 MHz and 25 °C. Electrical experiments are then performed by using the two-electrode method (stainless steel) and alternating current at a frequency of 120 Hz and a measurement voltage of 1 V, saturating the samples with brine (salinity of 56.5 g/L) and determining the conductivity σ (reciprocal of the resistivity Rt) by measuring the electric current. The electrode polarization effect associated with this two-electrode configuration is

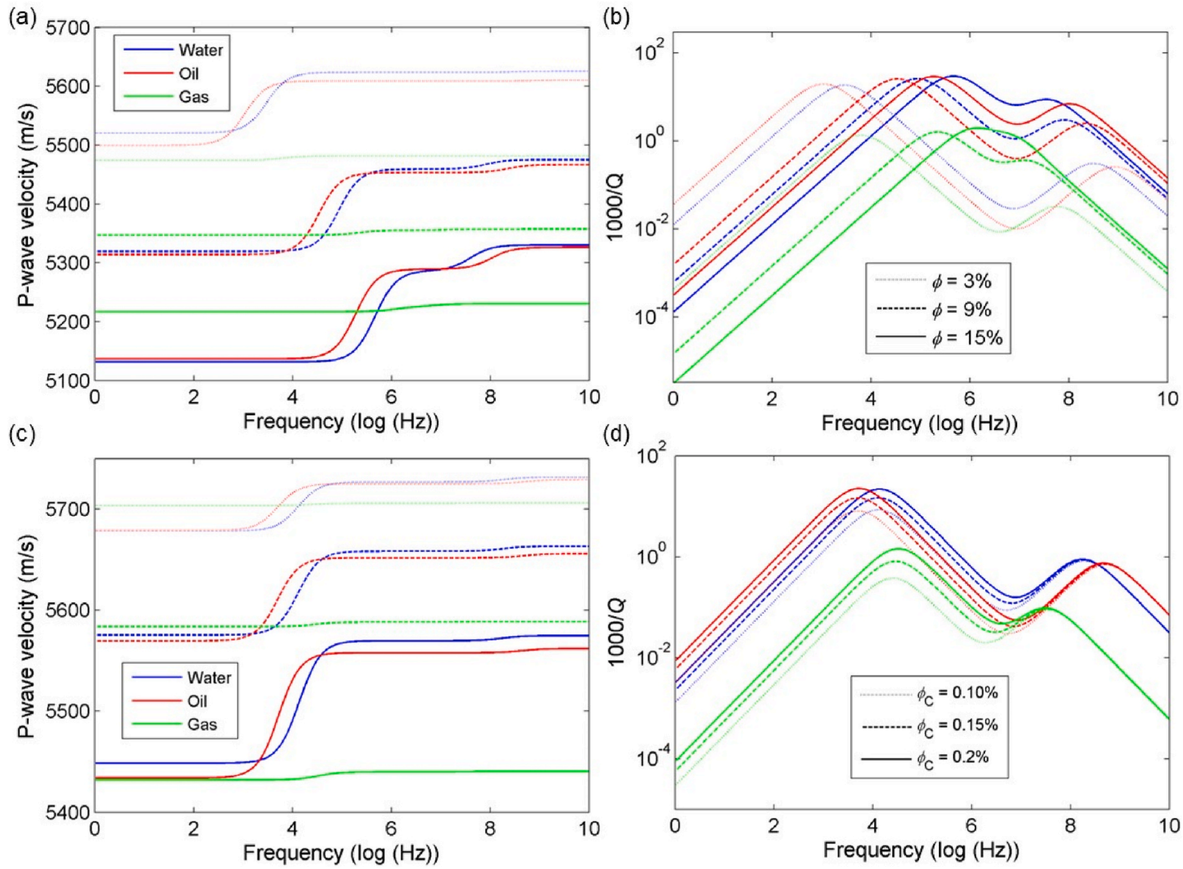

Fig. 11. P-wave velocity and attenuation as a function of frequency at different total (a and b) and microfracture (soft) porosities (c and d) and fluid types (a and c).

negligible at the low frequency and high salinity of brine that we used (Han et al., 2020; Pang et al., 2022).

2.3. Experimental results

Fig. 5a–f shows the porosity, microfracture-crack (soft) porosity, permeability, conductivity, and P- and S-wave velocities as a function of effective pressure (P_{eff}). The microfracture porosity is obtained as Shapiro (2003) (see Appendix A). Porosity and permeability vary exponentially at low pressures and become nearly linear as pressure increases (Fig. 5a and c). The soft porosity decreases exponentially with an increasing pressure (Fig. 5b). Sample B has a low porosity but a high conductivity, which can be explained by its high soft porosity (Fig. 5d). In comparison, sample D exhibits a lower soft porosity, lower conductivity and higher velocity. The wet-rock P-wave velocity is higher than that at dry conditions, while the dry-rock S-wave higher than the wet one due to the density effect (Fig. 5e–f).

Fig. 6 shows cross-property relations, where the colors represent the effective pressure. High porosity is associated with high permeability, while not appreciably with soft porosity. The properties change significantly at low pressures. Higher conductivity is associated with lower velocities and effective pressures. These experimental results show the acoustic, electrical and transport properties are related to the pore structure, which is correlated with pressure.

3. Digital rock physics

3.1. Multiphase segmentation approach

After removing the unclear areas at the edge of the samples, the dimensions of each CT scan are 1600 × 1600 × 1600 pixels and a resolution of 2.8 μm. A subvolume of 800^3 pixels is selected from the individual 3D datasets in the segmentation process. The purpose of the representative elemental volume (REV) is to select an appropriate size that can accurately characterize the rock microstructure while meeting storage and computational requirements. It is considered that REV can be adopted in the analyses on AE characteristics of rock (Saxena et al., 2019; Balcewicz et al., 2021; Khodaei et al., 2022; Siegert et al., 2022; Karimpouli et al., 2020, 2023). In addition to meeting these two conditions, the results of porosity and mineral experiments are also used as constraint conditions (Fig. 1) to obtain the appropriate REV.

Segmentation is performed. First, a non-local mean filter is applied for denoising with the following properties: spatial standard deviation: 3; intensity standard deviation: 0.05; search window: 10 pixels; local neighborhood: 5 pixels. Due to differences in image quality, these properties may vary for each sample. Then, a geologically oriented multistep segmentation workflow is applied, based on threshold segmentation of gray-scale intensities in the first step (Balcewicz et al., 2021). The workflow is based on individual and repeated application of the gray level threshold for each stage. In this way, the critical boundary regions in the grayscale histogram near two peaks, ideally reflecting the phase attenuation coefficients, are minimized. Segmentation takes into account geological diagenesis, mineral composition, sample microstructures, and porosity. Due to quality limitations, the final segmented volume must be limited to (1) pore, (2) quartz, (3) plagioclase, (4) K-feldspar, (5) dolomite, and (6) clay (Fig. 7).

After segmentation, the total and connected pore spaces are determined. A pore network model of Sample A indicates small pore voids connected by short pore throats (Fig. 8). This structure feature of a tight-oil sandstone is observed in all samples. The distributions of pore and

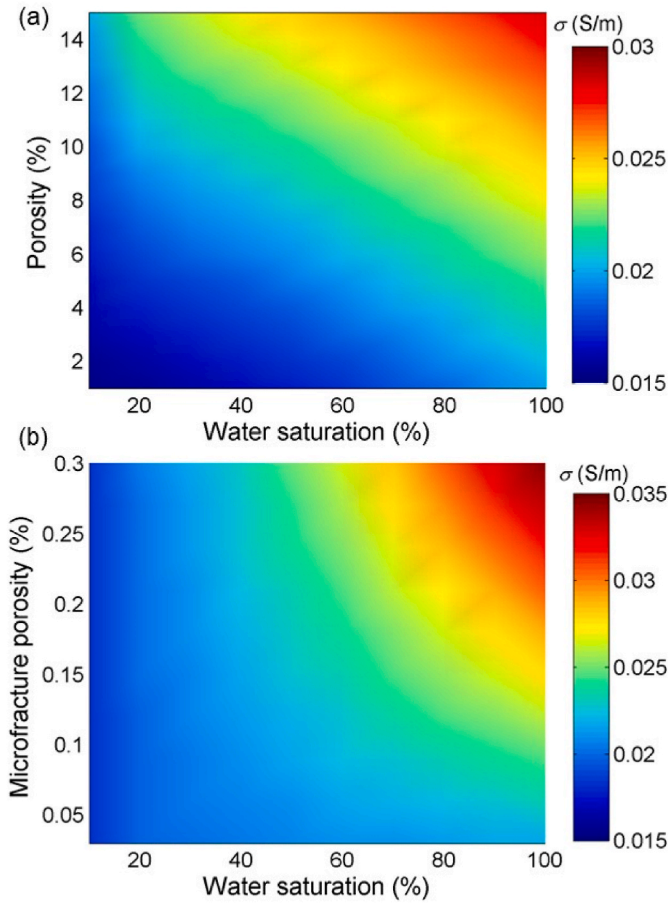

Fig. 12. Electrical conductivity as a function of porosity (a), and microfracture porosity (b) and water saturation.

throat radii of the samples are shown in Fig. 9, and indicate that the throat radius is mainly distributed in the range of 0–10 μm, which is smaller than the pore radius. Finally, each binary model is complemented by physical mineral properties (moduli and density) according to Mavko et al. (2009), resulting in a digital twin.

3.2. Numerical simulation

Numerical simulations based on the segmented digital twins are performed to compute the properties at the pore-scale. P- and S-wave velocities are obtained by using the rotated staggered finite difference grid method (Saenger and Bohlen, 2004; Saenger et al., 2004). Here, the velocities of elastic waves transmitting through a heterogeneous material at the long wavelength limit (pore size ≪ wavelength) are considered. Due to computational limitations, effective elastic properties are determined for 400^3 subvolumes (see Fig. 7a').

To simulate the permeabilities, the stationary Stokes equations are solved numerically by the finite volume method (Siegert et al., 2022). The numerical setup considers the full 800^3 resolution of each sample, but only the connected pore space is considered. Computations are performed for the x-, y-, and z-directions, with the equations given in Appendix B.

The stationary current continuity equation is numerically solved to obtain the conductivity (Karimpouli et al., 2023), and Ohm's law (Saslow, 2002) is applied. Numerical models with a resolution of 800^3 voxels are used, and the conductivity is simulated at the three principal directions (Appendix B). The local conductivities of the pore fluid and minerals are assigned to the corresponding voxels. We have for the fluid (water conductivity σ_W) and minerals (except for clay): 8.7 S/m and 10^{-6} S/m (Carcione and Seriani, 2000; Pang et al., 2022), respectively, and the conductivity of the clay minerals is $\sigma_{clay} = 0.2$ S/m (Lee, 2011; Pan et al., 2019).

The results are given in Table 2, showing the permeability and conductivity at the three principal directions and the P- and S-wave velocities at the z-direction.

4. Equivalent petrophysical models

We use an equivalent medium theory to describe the microstructure of tight-oil reservoir rocks, as shown in Fig. 10. The rock minerals (obtained by XRD) are considered as an equal mineral mixture, and the pores and microfractures-cracks are assumed ellipsoidal with different aspect ratios. The elastic-electrical Hashin-Shtrikman (HS), DEM and wave propagation equations are used to compute the AE properties.

4.1. AE equivalent models

First, an acoustic EPM is established. The mineral composition is analyzed with an XRD test, and average HS bounds (Mavko et al., 2009) are used to estimate the elastic moduli of the mineral mixture. We consider a dual porosity model, assuming that the rock skeleton consists of a host medium and an inclusion phase containing stiff and soft pores, respectively, with different aspect ratios. The elastic DEM (Berryman, 1992) is employed to add pores and microfractures to the host and inclusion, respectively, and then add the inclusions to the host phase to obtain equivalent dry-rock moduli. Then, the Biot-Rayleigh equations (Ba et al., 2011) give the wet-rock moduli and velocities (see Appendix C).

On the other hand, the conductivity of the mineral mixture is given with average electrical HS bounds (Mavko et al., 2009). The electrical DEM (Cilli and Chapman, 2021) is applied to add pores and microfractures containing fluids into the minerals, and the same pore structure (aspect ratios) as the acoustic model is assumed to estimate the conductivity (see Appendix D). The polarization effect is neglected (Pang et al., 2022), and the effect of frequency on the electrical properties is not considered.

4.2. AE responses

The model properties are given in Table 3. Fig. 11 shows the P-wave velocity and attenuation as a function of frequency, where we observe that with the increasing total and soft porosities, the P-wave velocity decreases and dispersion and attenuation (anelasticity) increase. The major anelasticity bands shift to the high frequencies with increasing total porosity. In the case of gas, the anelasticity is much weaker.

Table 4
Input properties to the acoustic and electrical EPMs.

Samples	φ (%)	φ_C (%)	R_0 (μm)	K_S (GPa)	G_S (GPa)	σ_S (S/m)	α_0	α_C
A	4.92	0.31004	10	43.4	30.1	0.0128	0.5	0.0006
B	6.71	0.45001	10	47.3	32.5	0.0182	0.5	0.0006
C	8.22	0.21756	10	45.9	30.7	0.0261	0.5	0.0006
D	8.44	0.1532	10	45.3	32.8	0.0216	0.5	0.0006

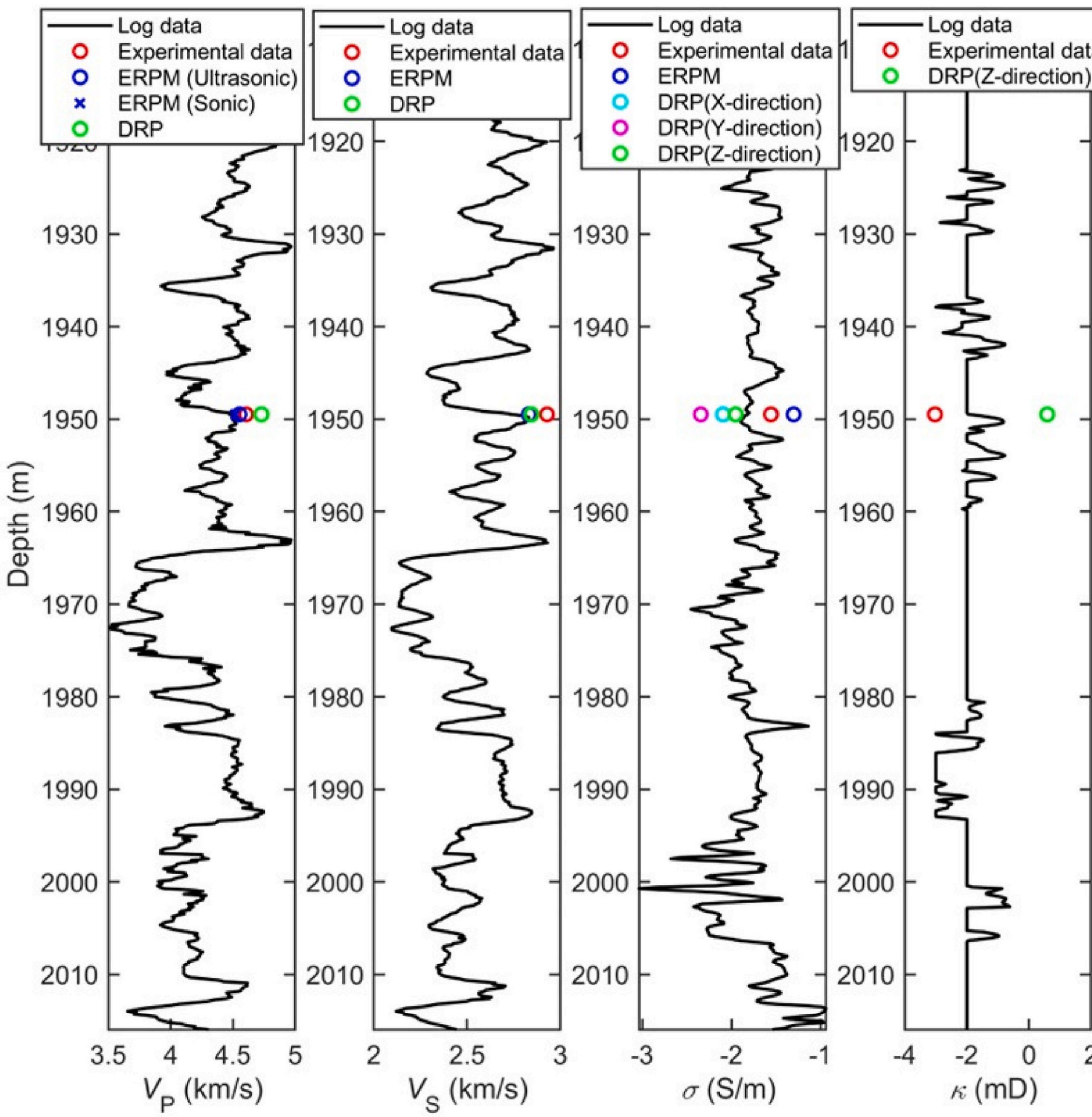

Fig. 13. Comparison among EPM and DRP simulations and log (Well A) and experimental (laboratory) data for sample A. (a) P-wave velocity, (b) S-wave velocity, (c) electrical conductivity and (d) permeability.

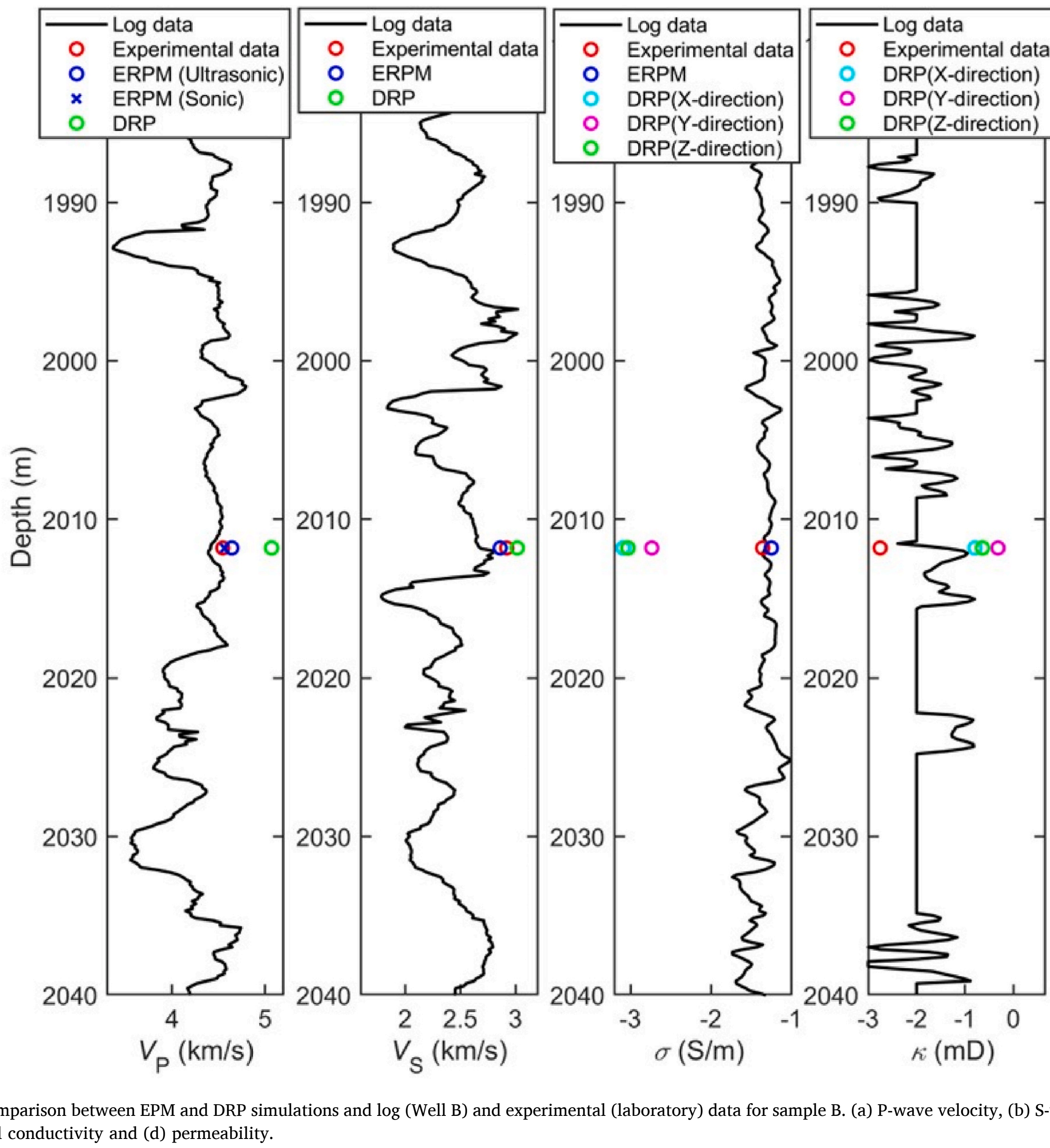

Fig. 14. Comparison between EPM and DRP simulations and log (Well B) and experimental (laboratory) data for sample B. (a) P-wave velocity, (b) S-wave velocity, (c) electrical conductivity and (d) permeability.

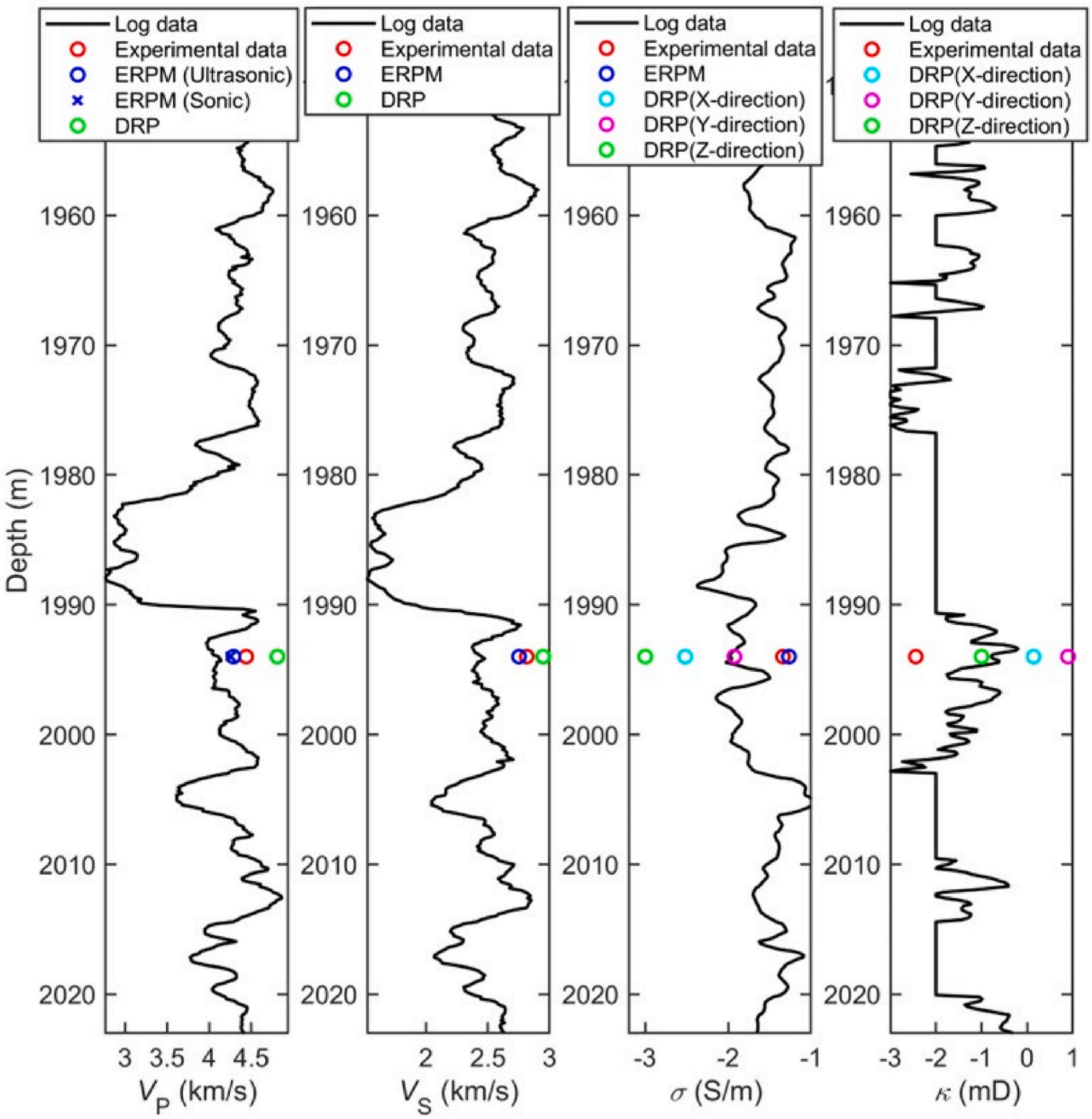

Fig. 15. Comparison between EPM and DRP simulations and log (Well C) and experimental (laboratory) data for sample C. (a) P-wave velocity, (b) S-wave velocity, (c) electrical conductivity and (d) permeability.

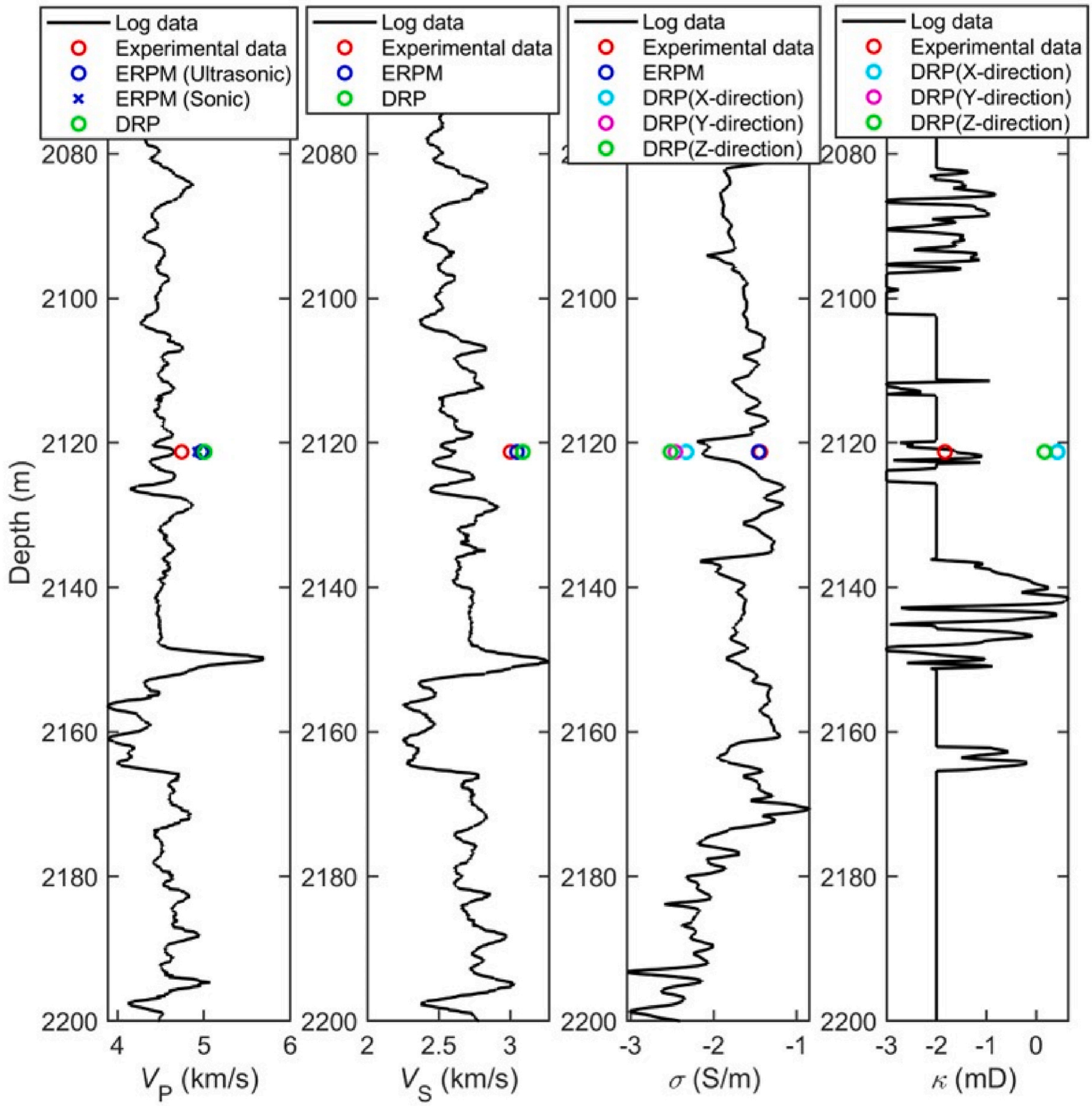

Fig. 16. Comparison between EPM and DRP simulations and log (Well D) and experimental (laboratory) data for sample D. (a) P-wave velocity, (b) S-wave velocity, (c) electrical conductivity and (d) permeability.

Table 5
Multiscale parameters of the acoustic model.

Scale	Frequency	R_0	κ_0	φ_C (%)	α_0	α_C
Ultrasonic	0.55 MHz	10 μm	25 mD	0.3	0.5	0.0006
Sonic	10 kHz	1 mm	25 D	0.3	0.5	0.0006
Seismic	35 Hz	10 mm	50 D	0.3	0.5	0.0006

Similarly, Fig. 12 shows the electrical response as a function of the stiff and soft porosity and saturation. The conductivity increases when these quantities increase, indicating that a strong relation to the pore structure and fluid content.

5. Comparison between theory and experimental data

To verify the performance of the EPM and DRP approaches, results at in-situ conditions (effective and pore pressures of 15 MPa) and well-log data are compared. The total and soft porosities in the AE models and other properties are given in Table 4.

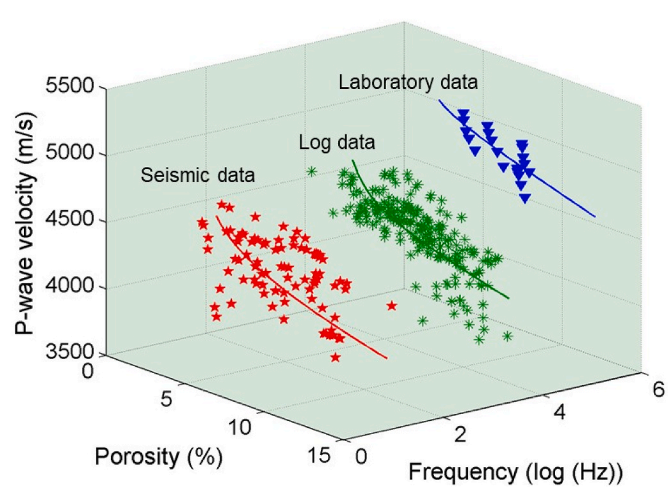

Fig. 17. P-wave velocities as a function of frequency and porosity compared with laboratory (ultrasonic), log, and seismic data.

Figs. 13–16 compare the DRP and EPM simulations with experimental (laboratory, circles) and well-log data (black lines). There is a dispersion effect at different scales, i.e., ultrasonic velocity is higher than sonic velocity (logs), as are conductivity values, while permeability is lower than well data. Similarly, we use EPM to simulate the P-wave velocity in the two frequency bands and analyze the dispersion, showing the same behavior as the data. The wave velocity generally agrees with those of the samples, while the conductivity and permeability show deviations from the measurements, which may be due to an incorrect estimation of the pore network.

Finally, we compare ultrasonic measurements, sonic log and seismic data, with the acoustic EPM. The simulation can be performed by adjusting the frequency and inclusion size of the acoustic model, as shown in Table 5. Fig. 17 shows the results. There is frequency dispersion and higher velocity at higher frequencies, and a good agreement between data and theory.

6. Conclusions

We have obtained thin sections of tight-oil reservoir cores to perform DRP images (XRD and CT scans) and ultrasonic and conductivity experiments as a function of differential pressure, saturation and fluid type, with the aim of investigating how mineralogy and pore structure affect the AE properties on the basis of EPMs. Experimental data show that tight-oil rocks have complex lithology characteristics (mineral components and pore structure) and their AE physical properties depend strongly on pressure and microstructure. Furthermore, we conclude.

- Given the complex lithology features of tight rocks, digital samples based on geologically oriented multiphase segmentation and multiple rock physics experiments can effectively characterize rock microstructures. In addition, DRP can be effectively used to simulate elastic and anelastic properties, but the simulation of conductivity and permeability depends significantly on the quality of the images.
- The joint EPMs are created by combining multiple tests and AE effective medium and wave propagation equations, which can effectively simulate the AE properties and link multiscale data, but the modeling must be able to describe the effects of soft porosity (microfractures and cracks) on the anelastic effects.
- This study successfully compares the AE properties obtained with DRP and EPM by using the multiscale data and opens ideas for combining the two approaches. In a future research, digital cores can be used to obtain accurate pore structure for EPM. In addition, DRP can be extended to characterize reservoir properties by referring to rock physics modeling.

Declaration of competing interest

The authors declare that they have no known competing financial interests or personal relationships that could have appeared to influence the work reported in this paper.

Data availability

Data will be made available on request.

Acknowledgements

This work is supported by the National Natural Science Foundation of China (grant no. 41974123, 42174161), and the Jiangsu Province Science Fund for Distinguished Young Scholars (grant no. BK20200021). Experimental waveform and electrical and CT scan data associated with this article can be accessed at https://doi.org/10.5281/zenodo.7903718.

Appendix A. Microfracture porosity estimation

As the effective pressure increases, microfractures and cracks gradually tend to close, leaving only the stiff pores. The total porosity is

$$\varphi = \varphi_S + \varphi_C \tag{A-1}$$

(Shapiro, 2003), where φ_S and φ_C are the stiff and microfracture/crack (soft) porosities, respectively. Figure A1 shows the total porosity as a function of the effective pressure, with exponential and linear fits at high pressures to obtain the stiff and soft porosities at different pressures.

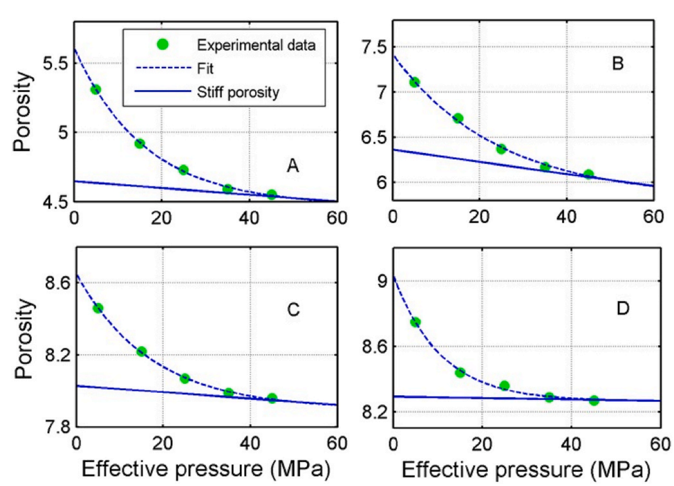

Fig. A1. Total porosity and simulated stiff porosity of the samples at different effective pressures.

Appendix B. Simulation of the permeability and electrical conductivity

For each direction, we simulate the original Darcy experiment (Darcy, 1856) by considering a model of length L and area A, where a volume flux Q

circulates between two opposite sides, defined as inlet and outlet, having a pressure difference Δp. The remaining faces of the model have no flow. The induced flow is obtained with the stationary Stokes equations,

$$\nabla \cdot \mathbf{V} = 0 \tag{B-1}$$

$$\nabla \cdot (\eta \nabla \mathbf{V}) = \nabla p \tag{B-2}$$

where $\mathbf{V}$ is the velocity field and p is the associated pressure field. The volumetric flow rate is

$$Q = \int_{A_{outlet}} \mathbf{V} dA = -\int_{A_{inlet}} \mathbf{V} dA \tag{B-3}$$

The permeability is given by Darcy law (Darcy, 1856),

$$\kappa = \frac{Q \cdot \eta \cdot L}{A \cdot \Delta p} \tag{B-4}$$

where η is the dynamic fluid viscosity.

A similar procedure is used to calculate the electrical conductivity. At the beginning of each simulation, a potential difference $\Delta\varphi$ is specified as a boundary condition between two opposite sides (i.e., inlet and outlet) and the local conductivity field of each phase is set according to the respective sample mineral structure. By solving the current continuity equation,

$$\nabla \cdot (\sigma \nabla \varphi) = 0 \tag{B-5}$$

The electric current I is

$$I = -\int_{A_{outlet}} \sigma \nabla \varphi dA = \int_{A_{inlet}} \sigma \nabla \varphi dA \tag{B-6}$$

and Ohm's law (Saslow, 2002) gives the conductivity

$$\sigma = \frac{I \cdot L}{A \cdot \Delta \varphi} \tag{B-7}$$

Appendix C. Acoustic EPM

Berryman (1992) proposed the following DEM equations to compute the dry-rock bulk and shear moduli of the host (K_{b1}, μ_{b1}), inclusion (K_{b2}, μ_{b2}) and rock skeleton (K_b, μ_b),

$$(K_2 - K^*)P^{(*2)}(y) = (1-y)\frac{\mathrm{d}}{\mathrm{dy}}[K^*(y)] \tag{C-1}$$

$$(\mu_2 - \mu^*)Q^{(*2)}(y) = (1-y)\frac{\mathrm{d}}{\mathrm{dy}}[\mu^*(y)] \tag{C-2}$$

with initial conditions $K^*(0) = K_1$, and $\mu^*(0) = \mu_1$, where K_1 and μ_1 are the bulk and shear moduli of the host material, respectively, y is the content of phase 2, and K_2 and μ_2 are the corresponding moduli. P^{*i} and Q^{*i} are geometrical factors of the ith component (see Berryman, 1980; Mavko et al., 2009).

The wet-rock moduli and velocities are obtained from Ba et al. (2011), i.e., the double-porosity Biot-Rayleigh equations,

$$\begin{aligned} &N\nabla^2\mathbf{u} + (A+N)\nabla\varepsilon + Q_1\nabla\left(\zeta^{(2)} + \varphi_1\varsigma\right) + Q_2\nabla\left(\zeta^{(2)} - \varphi_1\varsigma\right) \\ &= \rho_{00}\ddot{\mathbf{u}} + \rho_{01}\ddot{\mathbf{U}}^{(1)} + \rho_{02}\ddot{\mathbf{U}}^{(2)} + b_1\left(\dot{\mathbf{u}} - \dot{\mathbf{U}}^{(1)}\right) + b_2\left(\dot{\mathbf{u}} - \dot{\mathbf{U}}^{(2)}\right) \end{aligned} \tag{C-3}$$

$$Q_1\nabla\varepsilon + R_1\nabla\left(\zeta^{(1)} + \varphi_2\varsigma\right) = \rho_{01}\ddot{\mathbf{u}} + \rho_{11}\ddot{\mathbf{U}}^{(1)} - b_1\left(\ddot{\mathbf{u}} - \ddot{\mathbf{U}}^{(1)}\right) \tag{C-4}$$

$$Q_2\nabla\varepsilon + R_2\nabla\left(\zeta^{(2)} - \varphi_1\varsigma\right) = \rho_{02}\ddot{\mathbf{u}} + \rho_{22}\ddot{\mathbf{U}}^{(2)} - b_2\left(\ddot{\mathbf{u}} - \ddot{\mathbf{U}}^{(2)}\right) \tag{C-5}$$

$$\begin{aligned} &\varphi_2\left(Q_1\varepsilon + R_1\left(\zeta^{(1)} + \varphi_2\varsigma\right)\right) - \varphi_1\left(Q_2\varepsilon + R_2\left(\zeta^{(2)} - \varphi_1\varsigma\right)\right) \\ &\qquad = \frac{1}{3}\rho_f\ddot{\varsigma}R_0^2\frac{\varphi_1^2\varphi_2\varphi_{20}}{\varphi_{10}} + \frac{1}{3}\frac{\eta\varphi_1^2\varphi_2\varphi_{20}}{\kappa_1}\dot{\varsigma}R_0^2 \end{aligned} \tag{C-6}$$

where, $\mathbf{u}$, $\mathbf{U}^{(1)}$ and $\mathbf{U}^{(2)}$ are the displacement vectors of the frame, host fluid and inclusion fluid, respectively, and ε, $\zeta^{(1)}$ and $\zeta^{(2)}$ are the corresponding divergences. The scalar ς represents the fluid variation in the local fluid flow, v_1 and v_2 are the volume ratios of the host medium and inclusions ($v_1 + v_2 = 1$), respectively, φ_1 and φ_2 are the corresponding absolute porosities ($\varphi_1 + \varphi_2 = \varphi$), $\varphi_1 = v_1\varphi_{10}$, and $\varphi_2 = v_2\varphi_{20}$, where φ_{10} and φ_{20} are the local porosities of the host and inclusions, respectively, ρ_f is the fluid density, η is the viscosity, κ_1 is the host permeability, A, N, R_1, R_2, Q_1, and Q_2 are stiffnesses coefficients, R_0 is the inclusion radius, ρ_{00}, ρ_{01}, ρ_{02}, ρ_{11} and ρ_{22} are density coefficients, and b_1 and b_2 represent Biot's dissipation coefficients.

The complex wave number k is obtained by substituting a plane P-wave kernel into equations (C3-6) and solving the dispersion equation

$$\begin{vmatrix} a_{11}k^2+b_{11} & a_{12}k^2+b_{12} & a_{13}k^2+b_{13} \\ a_{21}k^2+b_{21} & a_{22}k^2+b_{22} & a_{23}k^2+b_{23} \\ a_{31}k^2+b_{31} & a_{32}k^2+b_{32} & a_{33}k^2+b_{33} \end{vmatrix} = 0 \tag{C-7}$$

where,

$$\begin{aligned}
&a_{11}=A+2N+\mathrm{i}(Q_2\varphi_1-Q_1\varphi_2)x_1, b_{11}=-\rho_{00}\omega^2+\mathrm{i}\omega(b_1+b_2)\\
&a_{12}=Q_1+\mathrm{i}(Q_2\varphi_1-Q_1\varphi_2)x_2, b_{12}=-\rho_{01}\omega^2-\mathrm{i}\omega b_1\\
&a_{13}=Q_2+\mathrm{i}(Q_2\varphi_1-Q_1\varphi_2)x_3, b_{13}=-\rho_{02}\omega^2-\mathrm{i}\omega b_2\\
&a_{21}=Q_1-\mathrm{i}R_1\varphi_2x_1, b_{21}=b_{12}\\
&a_{22}=R_1-\mathrm{i}R_1\varphi_2x_2, b_{22}=-\rho_{11}\omega^2+\mathrm{i}\omega b_1\\
&a_{23}=-\mathrm{i}R_1\varphi_2x_3, b_{23}=0\\
&a_{31}=Q_2+\mathrm{i}R_2\varphi_1x_1, b_{31}=b_{13}\\
&a_{32}=\mathrm{i}R_2\varphi_1x_2, b_{32}=0\\
&a_{33}=R_2+\mathrm{i}R_2\varphi_1x_3, b_{33}=-\rho_{22}\omega^2+\mathrm{i}\omega b_2
\end{aligned} \tag{C-8}$$

and,

$$\begin{aligned}
&x_1=\mathrm{i}(\varphi_2Q_1-\varphi_1Q_2)/Z\\
&x_2=\mathrm{i}\varphi_2R_1/Z\\
&x_3=-\mathrm{i}\varphi_1R_2/Z
\end{aligned} \tag{C-9}$$

$$Z=\frac{\mathrm{i}\omega\eta\varphi_1^2\varphi_2\varphi_{20}R_0^2}{3\kappa_1}-\frac{\rho_f\omega^2R_0^2\varphi_1^2\varphi_2\varphi_{20}}{3\varphi_{10}}-\left(\varphi_2^2R_1+\varphi_1^2R_2\right) \tag{C-10}$$

The Biot dissipation coefficients (Biot, 1962; Ba et al., 2011) and the permeabilities of the two phases (Mavko et al., 2009) are

$$b_1=\varphi_1\varphi_{10}\frac{\eta_f}{\kappa_1},\quad b_2=\varphi_2\varphi_{20}\frac{\eta_f}{\kappa_2} \tag{C-11}$$

$$\kappa_1=\frac{\kappa_0\varphi_1^3}{(1-\varphi_1)^2},\quad \kappa_2=\frac{\kappa_0\varphi_2^3}{(1-\varphi_2)^2} \tag{C-12}$$

where $\kappa_0 = 25$ mdarcy (mD). The stiffness and density coefficients are

$$A=(1-\varphi)K_s-\frac{2}{3}N-\frac{K_s}{K_f}(Q_1+Q_2),\quad N=\mu_b \tag{C-13}$$

$$Q_1=\frac{\varphi_1\beta K_s}{\beta+\gamma},\quad Q_2=\frac{\varphi_2K_s}{1+\gamma} \tag{C-14}$$

$$R_1=\frac{\varphi_1K_f}{\beta/\gamma+1},\quad R_2=\frac{\varphi_2K_f}{1+1/\gamma} \tag{C-15}$$

$$\gamma=\frac{K_s}{K_f}\frac{\varphi_1\beta+\varphi_2}{(1-\varphi)-K_b/K_s} \tag{C-16}$$

$$\rho_{00}=(1-\varphi)\rho_s-\frac{1}{2}(\varphi-1)\rho_f \tag{C-17}$$

$$\rho_{01}=\frac{1}{2}(\varphi_1-v_1)\rho_f,\quad \rho_{02}=\frac{1}{2}(\varphi_2-v_2)\rho_f \tag{C-18}$$

$$\rho_{11}=\frac{1}{2}(\varphi_1+v_1)\rho_f,\quad \rho_{22}=\frac{1}{2}(\varphi_2+v_2)\rho_f \tag{C-19}$$

where, K_s and K_f are the bulk moduli of the mineral mixture (obtained with the HS average) and fluid, respectively, K_b and μ_b are the elastic moduli of the skeleton (obtained with the DEM equations), and ρ_s and ρ_f are the densities corresponding to the mineral mixture and fluid, respectivley.

$$\beta = \frac{Q_1 R_2}{Q_2 R_1} = \frac{\varphi_{20}}{\varphi_{10}} \left[\frac{1 - (1 - \varphi_{10}) K_s / K_{b1}}{1 - (1 - \varphi_{20}) K_s / K_{b2}} \right] \tag{C-20}$$

where K_{b1} and K_{b2} are the skeleton bulk moduli of the host and microfracture inclusions, respectively, which are computed by adding stiff and soft pores with the DEM equations, respectively.

The P-wave velocity and quality factor can be expressed (Carcione, 2022) as,

$$V_P = \left[\mathrm{Re}\left(v^{-1}\right) \right]^{-1} \tag{C-21}$$

$$Q = \frac{\mathrm{Re}(v^2)}{\mathrm{Im}(v^2)} \tag{C-22}$$

where $v = \omega / k$ is the complex velocity and ω is the angular frequency.

Appendix D. Electrical EPM

Electrical DEM is proposed by Cilli and Chapman (2021) to obtained the rock conductivity,

$$(\sigma_2 - \sigma^*)\lambda = (1 - y)\frac{d}{dy}[\sigma^*(y)] \tag{D-1}$$

with initial conditions $\sigma^*(0) = \sigma_1$, where σ_1 is the conductivity of the host phase. σ_2 is the conductivity of phase 2, that is the conductivity of the pores and microcracks, corresponding to R_W when water saturation is 1 (Aguilera and Aguilera, 2003), and

$$\lambda = \frac{1}{3} \sum_{p=1}^{3} \left\{ \left[1 + \left(\frac{\sigma_2}{\sigma^*} - 1 \right) L_P \right]^{-1} \right\} \tag{D-2}$$

where L_P (P = 1, 2, 3) is the depolarizing factor of phase 2 (Osborn, 1945; Asami, 2002). We consider ellipsoid inclusions of aspect ratio $\alpha < 1$,

$$L_3 = \frac{1}{1 - \alpha^2} - \frac{\alpha}{(1 - \alpha^2)^{3/2}} \cos^{-1} \alpha \tag{D-3}$$

$$L_1 = L_2 = (1 - L_3) / 2 \tag{D-4}$$

According to Archie's equation (1942), the conductivity of pores and microfractures as a function of water saturation is,

$$\sigma_2 = \gamma^{-1} S_W^2 \sigma_W \tag{D-5}$$

where σ_W is the brine conductivity, n is a saturation exponent and γ is a lithology coefficient.

References

Aguilera, M.S., Aguilera, R., 2003. Improved models for petrophysical analysis of dual porosity reservoirs. Petrophysics 44 (1).

Andrä, H., Combaret, N., Dvorkin, J., Glatt, E., Han, J., Kabel, M., Keehm, Y., Krzikalla, F., Lee, M., Madonna, C., Marsh, M., Mukerji, T., Saenger, E.H., Sain, R., Saxena, N., Ricker, S., Wiegmann, A., Zhan, X., 2013a. Digital rock physics benchmarks—Part I: imaging and segmentation. Comput. Geosci. 50, 25–32. https://doi.org/10.1016/j.cageo.2012.09.005.

Andrä, H., Combaret, N., Dvorkin, J., Glatt, E., Han, J., Kabel, M., Keehm, Y., Krzikalla, F., Lee, M., Madonna, C., Marsh, M., Mukerji, T., Saenger, E.H., Sain, R., Saxena, N., Ricker, S., Wiegmann, A., Zhan, X., 2013b. Digital rock physics benchmarks—part II: computing effective properties. Comput. Geosci. 50, 33–43. https://doi.org/10.1016/j.cageo.2012.09.008.

Alqahtani, N.J., Chung, T., Wang, Y.D., 2021. Flow-based characterization of digital rock images using deep learning. Armstrong, R.T., Swietojanski, P., Mostaghimi, P. SPE J. 26, 1800–1811.

Amalokwu, K., Best, I.A., Sothcott, J., Chapman, M., Minshull, T., Li, Y., 2014. Water saturation effects on elastic wave attenuation in porous rocks with aligned fractures. Geophys. J. Int. 197, 943–947.

Archie, G.E., 1942. The electrical resistivity log as an aid in determining some reservoir characteristics. Transactions of the AIME 146, 54–62. https://doi.org/10.2118/942054-G.

Asami, K., 2002. Characterization of heterogeneous systems by dielectric spectroscopy: progress in Polymer Science, 27, 1617–1659. https://doi.org/10.1016/S0079-6700(02)00015-1.

Ba, J., Carcione, J.M., Nie, J., 2011. Biot-Rayleigh theory of wave propagation in double-porosity media. J. Geophys. Res. 116, B06202 https://doi.org/10.1029/2010JB008185.

Ba, J., Cao, H., Carcione, J.M., Tang, G., Yan, X., Sun, W., Nie, J., 2013a. Multiscale rock-physics templates for gas detection in carbonate reservoirs: Journal of Applied Geophysics, 93, 77–82. https://doi.org/10.1016/j.jappgeo.2013.03.011.

Ba, J., Yan, X., Chen, Z., Xu, G., Bian, C., Cao, H., Yao, F., Sun, W., 2013b. Rock physics model and gas saturation inversion for heterogeneous gas reservoirs. Chin. J. Geophys. 56, 1696–1706. https://doi.org/10.6038/cjg20130527.

Ba, J., Xu, W., Fu, L., Carcione, J., Zhang, L., 2017. Rock anelasticity due to patchy-saturation and fabric heterogeneity: a double-double porosity model of wave propagation: Journal of Geophysical Research. Solid Earth 122 (3), 1949–1976. https://doi.org/10.1002/2016JB013882.

Balcewicz, M., Siegert, M., Gurris, M., Ruf, M., Krach, D., Steeb, H., Saenger, E.H., 2021. Digital rock physics: a geological driven workflow for the segmentation of anisotropic ruhr sandstone. Front. Earth Sci. 9, 493.

Berryman, J.G., 1980. Long-wavelength propagation in composite elastic media: Journal of Acoustical Society of America, 68 (6), 1809–1831.

Berryman, J.G., 1992. Single-scattering approximations for coefficients in Biot's equations of poroelasticity. Acoustical Society of America Journal 91 (2), 551–571.

Biot, M.A., 1962. Mechanics of deformation and acoustic propagation in porous media. J. Appl. Phys. 33, 1482–1498.

Blunt, M.J., Bijeljic, B., Dong, H., Gharbi, O., Iglauer, S., Mostaghimi, P., Paluszny, A., Pentland, C., 2013. Pore-scale imaging and modelling. Adv. Water Resour. 51, 197–216. https://doi.org/10.1016/j.advwatres.2012.03.003.

Bultreys, T., Van Offenwert, S., Goethals, W., Boone, M.N., Aelterman, J., Cnudde, V., 2022. X-ray tomographic micro-particle velocimetry in porous media. Phys. Fluids 34 (4), 042008.

Carcione, J.M., 2022. Wavefields in Real Media. Theory and Numerical Simulation of Wave Propagation in Anisotropic, Anelastic, Porous and Electromagnetic Media, 4rd ed. Elsevier.

Carcione, J.M., Gei, D., Picotti, S., Michelini, A., 2012. Cross-hole electromagnetic and seismic modeling for CO2 detection and monitoring in a saline aquifer. J. Petrol. Sci. Eng. 100, 162–172.

Carcione, J.M., Avseth, P., 2015. Rock-physics templates for clay-rich source rocks: geophysics, 80 (5), D481–D500. https://doi.org/10.1190/GEO2014-0510.1.
Carcione, J.M., Seriani, G., 2000. An electromagnetic modelling tool for the detection of hydrocarbons in the subsoil. Geophys. Prospect. 48 (2), 231–256.
Carcione, J.M., Ursin, B., Nordskag, J.I., 2007. Cross-property relations between electrical conductivity and the seismic velocity of rocks. Geophysics 72 (5), E193–E204.
Cartwright-Taylor, A., Mangriotis, M.D., Main, I.G., 2022. Seismic events miss important kinematically governed grain scale mechanisms during shear failure of porous rock. Nat. Commun. 13, 6169.
Chapman, S., Tisato, N., Quintal, B., Holliger, K., 2016. Seismic attenuation in partially saturated Berea sandstone submitted to a range of confining pressures. J. Geophys. Res. Solid Earth 121 (3), 1664–1676.
Cilli, P., Chapman, M., 2020. The power-law relation between inclusion aspect ratio and porosity: implications for electrical and elastic modeling. J. Geophys. Res. Solid Earth 125 (5), 1–25.
Cilli, P., Chapman, M., 2021. Linking elastic and electrical properties of rocks using cross-property DEM. Geophys. J. Int. 225, 1812–1823.
Darcy, H., 1856. Les fontaines publiques de la ville de Dijon: Exposition et application des principes à suivre et des formules à employer dans les questions de distribution d'eau: Ouvrage terminé par un appendice relatif aux fournitures d'eau de plusieurs villes, au filtrage des eaux et à la fabrication des tuyaux de fonte, de plomb, de tôle et de bitumen.
Deng, J., Wang, H., Zhou, H., Liu, Z., Song, L., Wang, X., 2015. Microtexture, seismic rock physical properties and modeling of Longmaxi Formation shale. Chin. J. Geophys. 58 (6), 2123–2136.
Gabàs, A., Macau, A., Benjumea, B., Queralt, P., Ledo, J., Figueras, S., Marcuello, A., 2016. Joint audio-magnetotelluric and passive seismic imaging of the Cerdanya Basin. Surv. Geophys. 37, 897–921. https://doi.org/10.1007/s10712-016-9372-4.
Golikov, P., Avseth, P., Stovas, A., Bachrach, R., 2012. Rock physics interpretation of heterogeneous and anisotropic turbidite reservoirs. In: Geophysical Prospecting, vol. 61. 2-Rock Physics for Reservoir Exploration, Characterisation and Monitoring), pp. 448–457.
Guo, J., Gurevich, B., Chen, X., 2022a. Dynamic SV wave signatures of fluid saturated porous rocks containing intersecting fractures: Journal of Geophysical Research: solid Earth, 127, e2022JB024745.
Guo, J., Zhao, L., Chen, X., Yang, Z., Li, H., Liu, C., 2022b. Theoretical modelling of seismic dispersion, attenuation, and frequency dependent anisotropy in a fluid saturated porous rock with intersecting fractures: geophysical Journal International, 230, 580–606.
Gupta, S.D., Chatterjee, R., Farooqui, M.Y., 2012. Rock physics template (RPT) analysis of well logs and seismic data for lithology and fluid classification in Cambay Basin. Int. J. Earth Sci. 101, 1407–1426. https://doi.org/10.1007/s00531-011-0736-1.
Han, T., 2018. Joint elastic-electrical properties of artificial porous sandstone with aligned fractures. Geophys. Res. Lett. 45 (7), 3051–3058.
Han, T., Best, A., Sothcott, J., MacGregor, L., 2011. Joint elastic-electrical properties of reservoir sandstones and their relationships with petrophysical parameters. Geophys. Prospect. 59, 518–535.
Han, T., Wei, Z., Li, F., 2020. How the effective pore and grain shapes are correlated in Berea sandstones: implications for joint elastic-electrical modeling. Geophysics 85 (3), MR147–MR154.
Jangda, Z., Menke, H., Busch, A., Geiger, S., Bultreys, T., Lewis, H., Singh, K., 2023. Pore-scale visualization of hydrogen storage in a sandstone at subsurface pressure and temperature conditions: trapping, dissolution and wettability. J. Colloid Interface Sci. 629, 316–325. Part B.
Jensen, E.H., Gelius, L.J., Johansen, T.A., Wang, Z., 2013. Consistent joint elastic-electrical differential effective-medium modelling of compacting reservoir sandstones. Geophys. Prospect. 61 (4), 788–802.
Ji, X., Wang, H., Ge, Y., Liang, J., Xu, X., 2022. Empirical mode decomposition-refined composite multiscale dispersion entropy analysis and its application to geophysical well log data. J. Petrol. Sci. Eng. 208, 109495.
Jia, C., Zou, C., Li, J., Li, D., Zheng, M., 2012. Assessment criteria, main types, basic features and resource prospects of the tight oil in China: acta Petrolei Sinica (in Chinese), 33 (3), 343–350.
Kadyrov, R., Nurgaliev, D., Saenger, E.H., Balcewicz, M., Minebaev, R., Statsenko, E., Glukhov, M., Nizamova, A., Galiullin, B., 2022. Digital rock physics: defining the reservoir properties on drill cuttings. J. Petrol. Sci. Eng. 210, 110063.
Karimpouli, S., Faraji, A., Balcewicz, M., Saenger, E.H., 2020. Computing heterogeneous core sample velocity using Digital Rock Physics: a multiscale approach. Comput. Geosci. 135, 104378.
Karimpouli, S., Kadyrov, R., 2022. Multistep super resolution double-U-net (SRDUN) for enhancing the resolution of berea sandstone images. J. Petrol. Sci. Eng. 216, 110833.
Karimpouli, S., Kadyrov, R., Siegert, M., Saenger, E.H., 2023. Applicability of 2D algorithms in digital rocks physics for 3D characterization: an example of a machine learning based super resolution image generation. Acta Geophys. 1–14 https://doi.org/10.1007/s11600-023-01149-7.
Khodaei, P., Karimpouli, S., Balcewicz, M., Saenger, E.H., 2022. Computing wave velocity of rock sample using rock chips and cuttings. J. Petrol. Sci. Eng. 209, 109849.
Lee, M., 2011. Connectivity equation and shaly-sand correction for electrical resistivity. USGS Scientific Investigations Report 2011–5005, 9.
Li, X., Li, C., Li, B., Liu, X., Chao, Y., 2020. Response laws of rock electrical property and saturation evaluation method of tight sandstone. Petrol. Explor. Dev. 47 (1), 214–224.
Liu, Q., Li, P., Jin, Z., Sun, Y., Hu, G., Zhu, D., Liu, J., 2021. Organic-rich formation and hydrocarbon enrichment of lacustrine shale strata: a case study of Chang 7 Member. Sci. China Earth Sci. 65, 118–138.
Luo, C., Ba, J., Guo, Q., 2023. Probabilistic seismic petrophysical inversion with statistical double-porosity Biot-Rayleigh model. Geophysics 88 (3), M157–M171.
Ma, R., Ba, J., Carcione, M.J., Zhou, X., Li, F., 2019. Dispersion and attenuation of compressional waves in tight oil reservoirs: experiments and simulations. Appl. Geophys. 16 (1), 33–45.
Madonna, C., Quintal, B., Frehner, M., Almqvist, B.S., Tisato, N., Pistone, M., et al., 2013. Synchrotron-based X-ray tomographic microscopy for rock physics investigations Synchrotron-based rock images. Geophysics 78 (1), D53–D64.
Mavko, G., Mukerji, T., Dvorkin, J., 2009. The Rock Physics Handbook: Tools for Seismic Analysis of Porous Media. Cambridge University Press.
Menke, H.P., Maes, J., Geiger, S., 2021. Upscaling the porosity–permeability relationship of a microporous carbonate for Darcy-scale flow with machine learning. Sci. Rep. 11, 2625. https://doi.org/10.1038/s41598-021-82029-2.
Müller, T.M., Gurevich, B., Lebedev, M., 2010. Seismic wave attenuation and dispersion resulting from wave-induced flow in porous rocks-A review. Geophysics 75, 75A147–75A164. https://doi.org/10.1190/1.3463417.
Osborn, J.A., 1945. Demagnetizing factors of the general ellipsoid. Phys. Rev. 67 (11–12), 351.
Pan, H., Li, H., Grana, D., Zhang, Y., Liu, T., Geng, C., 2019. Quantitative characterization of gas hydrate bearing sediment using elastic-electrical rock physics models. Mar. Petrol. Geol. 105, 273–283.
Pang, M., Ba, J., Carcione, J.M., Balcewicz, M., Yue, W., Saenger, E.H., 2022. Acoustic and electrical properties of tight rocks: a comparative study between experiment and theory. Surv. Geophys. 1–31.
Pang, M., Ba, J., Carcione, J., Picotti, S., Zhou, J., Jiang, R., 2019. Estimation of porosity and fluid saturation in carbonates from rock-physics templates based on seismic Q. Geophysics 84 (6), M25–M36. https://doi.org/10.1190/geo2019-0031.1.
Pang, M., Ba, J., Carcione, J.M., Saenger, E.H., 2021a. Elastic-electrical rock-physics template for the characterization of tight-oil reservoir rocks. Lithosphere, 3341849.
Pang, M., Ba, J., Carcione, J., Zhang, L., Ma, R., Wei, Y., 2021b. Seismic identification of tight-oil reservoirs by using 3D rock-physics templates. J. Petrol. Sci. Eng. 201, 108476.
Paustian, R., Andersson, L., Helland, J.O., Wildenschild, D., 2021. On the relationship between capillary pressure, saturation, and interfacial area for three-phase flow in water-wet porous media. Adv. Water Resour. 151, 103905.
Picotti, S., Carcione, J.M., Ba, J., 2018. Rock-physics templates for seismic Q. Geophysics 84 (1), MR13–MR23.
Saenger, E.H., Gold, N., Shapiro, S.A., 2000. Modeling the propagation of elastic waves using a modified finite-difference grid. Wave Motion 31, 77–92.
Saenger, E.H., Bohlen, T., 2004. Finite-difference modeling of viscoelastic and anisotropic wave propagation using the rotated staggered grid. Geophysics 69, 583–591. https://doi.org/10.1190/1.1707078.
Saenger, E.H., Krüger, O.S., Shapiro, S.A., 2004. Numerical considerations of fluid effects on wave propagation. Geophys. Res. Lett. 31 (21), 163–183.
Saenger, E.H., Shapiro, S.A., Keehm, Y., 2005. Seismic effects of viscous Biot-coupling: finite difference simulations on micro-scale. Geophys. Res. Lett. 321 (14), 337–349.
Saenger, E.H., Vialle, S., Lebedev, M., Uribe, D., Osorno, M., Duda, M., Steeb, H., 2016. Digital carbonate rock physics. Solid Earth 7, 1185–1197. https://doi.org/10.5194/se-7-1185-2016.
Saslow, W.M., 2002. Ohm's law: electric current is driven by emf, and limited by electrical resistance. Electricity, Magnetism, and Light 281–335.
Saxena, N., Day-Stirrat, R.J., Hows, A., Hofmann, R., 2021. Application of deep learning for semantic segmentation of sandstone thin sections. Comput. Geosci. 152, 104778.
Saxena, N., Hofmann, R., Hows, A., Saenger, E.H., Duranti, L., Stefani, J., Wiegmann, A., Kerimov, A., Kabel, M., 2019. Rock compressibility from microcomputed tomography images: controls on digital rock simulations. Geophysics 84, WA127–WA139. https://doi.org/10.1190/GEO2018-0499.1.
Schlüter, S., Sheppard, A., Brown, K., Wildenschild, D., 2014. Image processing of multiphase images obtained via X-ray microtomography: a review. Water Resour. Res. 50, 3615–3639. https://doi.org/10.1002/2014WR015256.
Shapiro, S.A., 2003. Elastic piezosensitivity of porous and fractured rocks. Geophysics 68 (2), 482–486.
Shi, J., Zou, Y., Cai, Y., Zhan, Z., Sun, J., Liang, T., Peng, P., 2022. Organic matter enrichment of the Chang 7 member in the Ordos Basin: insights from chemometrics and element geochemistry. Mar. Petrol. Geol. 135, 105404.
Siegert, M., Gurris, M., Lebedev, M., Saenger, E.H., 2022. Numerical modeling of the permeability in Bentheim sandstone under confining pressure. Mar. Petrol.
Solazzi, S.G., Guarracino, L., Rubino, J.G., Holliger, K., 2019. Saturation hysteresis effects on the seismic signatures of partially saturated heterogeneous porous rocks. J. Geophys. Res. 124 (11), 11316–11335.
Spurin, C., Armstrong, R.T., McClure, J., Berg, S., 2023. Dynamic mode decomposition for analysing multi-phase flow in porous media. Adv. Water Resour. 175, 104423.
Sun, H., Duan, L., Liu, L., Fan, W., Fan, D., Yao, J., Zhao, J., 2019. The influence of micro-fractures on the flow in tight oil reservoirs based on pore-network models. Energies 12 (21), 4104.
Tan, M., Su, M., Liu, W., Song, X., Wang, S., 2021. Digital core construction of fractured carbonate rocks and pore-scale analysis of acoustic properties. J. Petrol. Sci. Eng. 196, 107771.
Wang, H., Liao, X., Zhao, X., 2015. Study of tight oil reservoir flow regimes in different treated horizontal well. J. Energy Inst. 88 (2).
Wang, P., Cui, Y., Liu, J., 2022a. Fluid discrimination based on inclusion-based method for tight sandstone reservoirs. Surv. Geophys. 43 (5), 1469–1496.

Wang, P., Li, J., Chen, X., Cui, Y., Wang, E., Yan, G., 2021. Extending the inclusion-based effective medium model with fluid pressures caused by wave-induced flow. Int. J. Rock Mech. Min. Sci. 145, 104849.
Wang, S., Tan, M., Wang, X., Zhang, L., 2022b. Microscopic response mechanism of electrical properties and saturation model establishment in fractured carbonate rocks. J. Petrol. Sci. Eng. 208, 109429.
Wildenschild, D., Vaz, C.M.P., Rivers, M.L., Rikard, D., Christensen, B.S.B., 2002. Using X-ray computed tomography in hydrology: systems, resolutions, and limitations. J. Hydrol. 267, 285–297. https://doi.org/10.1016/S0022-1694(02)00157-9.
Zhang, L., Ba, J., Carcione, J.M., 2021. Wave propagation in infinituple-porosity media. J. Geophys. Res. Solid Earth 126 (4), e2020JB021266.
Zhang, L., Ba, J., Carcione, J.M., et al., 2022. Seismic wave propagation in partially saturated rocks with a fractal distribution of fluid-patch size. J. Geophys. Res. Solid Earth 127 (2), e2021JB023809.
Zhou, S., Liu, D., Cai, Y., Yao, Y., Li, Z., 2017. 3D characterization and quantitative evaluation of pore-fracture networks of two Chinese coals using FIB-SEM tomography. Int. J. Coal Geol. 174, 41–54.
Zhou, S., Yan, G., Xue, H., Guo, W., Li, X., 2016. 2D and 3D nanopore characterization of gas shale in Longmaxi formation based on FIB-SEM. Mar. Petrol. Geol. 73, 174–180.